Tonotopy is not preserved in a descending stage of auditory cortex

Miaoqing Gu[1,2,10], Shanshan Liang[3,10], Jiahui Zhu[2,3], Ruijie Li[3], Ke Liu[3], Xuanyue Wang[4], Frank Ohl[5,6,7], Yun Zhang[4], Xiang Liao[3,4], Chunqing Zhang[3], Hongbo Jia[1,5,9], Yi Zhou[2,8,*], Jianxiong Zhang[3,*], Xiaowei Chen[3,4,*]

[1]School of Physical Science and Technology, Guangxi University, Nanning 530004, China.

[2]Guangxi Key Laboratory of Special Biomedicine and Advanced Institute for Brain and Intelligence, School of Medicine, Guangxi University, Nanning, 530004, China

[3]Brain Research Center and State Key Laboratory of Trauma and Chemical Poisoning, Third Military Medical University, Chongqing 400038, China.

[4]Chongqing Institute for Brain and Intelligence, Guangyang Bay Laboratory, Chongqing 400064, China.

[5]Leibniz Institute for Neurobiology (LIN), Magdeburg, Germany.

[6]Insitute of Biology (IBIO), Otto-von-Guericke University, Magdeburg, Germany.

[7]Center for Behavioral Brain Sciences (CBBS), Magdeburg, Germany.

[8]Department of Neurobiology, Chongqing Key Laboratory of Neurobiology, School of Basic Medicine, Third Military Medical University, Chongqing 400038, China.

[9]Brain Research Instrument Innovation Center, Suzhou Institute of Biomedical Engineering and Technology, Chinese Academy of Sciences, Suzhou 215163, China

[10]These authors contributed equally to this work.

*Correspondence: yzhou@tmmu.edu.cn (Y.Z.), jianxiong_zhang1988@tmmu.edu.cn (J.Z.), xiaowei_chen@tmmu.edu.cn (X.C.)

Abstract

Previous studies based on layer specificity suggest that ascending signals from the thalamus to sensory neocortex preserve spatially organized information, but it remains unknown whether sensory information descending from sensory neocortex to thalamus also maintains such spatial organization pattern. By focusing on projection specificity, we mapped tone response properties of two groups of cortical neurons in the primary auditory cortex (A1), based on the relationship between their specific connections to other regions and their function in ascending (thalamocortical recipient, TR neurons) or descending (corticothalamic, CT neurons) auditory information. A clear tonotopic gradient was observed among TR, but not CT neurons. Additionally, CT neurons exhibited markedly higher heterogeneity in their frequency tuning and had broader bandwidth than TR neurons. These results reveal that the information flow descending from A1 to thalamus via CT neurons does not arrange tonotopically, suggesting that the descending information flow possibly contributes to higher-order feedback processing of diverse auditory inputs.

Introduction

In the mammalian auditory system, one of the most prominent features is the tonotopic organization — a spatially ordered gradient of neuronal frequency preference (Bizley et al., 2005; Kajikawa et al., 2005; Merzenich et al., 1976; Morel et al., 1993; Nelken et al., 2004; Reale and Imig, 1980; Stiebler et al., 1997; Tani et al., 2018). Clear tonotopic maps have been found in the auditory cortex (AuC) of many mammalian species including humans (Clopton et al., 1974; Humphries et al., 2010), macaque monkeys (Hackett et al., 1998), cats (Lee et al., 2004), ferrets (Bizley et al., 2005), Mongolian gerbils (Budinger et al., 2000; Ohl et al., 2000; Thomas et al., 1993), rats (Polley et al., 2007), and mice (Guo et al., 2012; King et al., 2018). Tonotopy originates in the cochlea and is relayed and preserved throughout all the ascending stages including the medial geniculate body (MGB) and the AuC (Jasmin et al., 2019; Simon et al., 2009; Smith and Wever, 1949). As one of the most explored pathways in the auditory system, the connections between MGB and AuC play an essential role in

the perception of auditory information (Lee, 2013; Ohga et al., 2017; Pardi et al., 2020).

Core fields of the AuC receive their predominant thalamic input from ventral division of the MGB (MGBv), which confers well-defined frequency tuning arranged into smoothly varying tonotopic gradients (Andersen et al., 1980; Merzenich and Brugge, 1973; Winer et al., 2005). Non-core AuC fields are innervated by non-primary divisions of the MGB and from intracortical inputs originating outside of the AuC (Jones, 2001; Lee and Winer, 2005; Reale and Imig, 1980), which show weak tonotopy and selectivity for processing conspecific communication sounds (Norman-Haignere et al., 2015; Schneider and Woolley, 2013). Feedforward auditory information is conveyed from the MGBv to the AuC, primarily received in layer 4 (L4) but also extending to other layers (Constantinople and Bruno, 2013; Petreanu et al., 2009). Subsequently, it is projected corticofugally to downstream targets from either layer 5 (L5) or layer 6 (L6) of the AuC (Shepherd and Yamawaki, 2021), including feedback information to MGB (Happel et al., 2014; Happel et al., 2010; Homma and Bajo, 2021; Kirchgessner et al., 2020). Several studies have revealed the sophisticated inputs and the ability in the perception of complex sounds of CT neurons in A1 (Clayton et al., 2021; Homma et al., 2017), suggesting the descending information flow in the core fields of the AuC possibly contributes to higher-order feedback processing of diverse auditory inputs.

It is also known that the tonotopic gradient is well preserved across all layers within the A1 (Guo et al., 2012; Montes-Lourido et al., 2021; Tischbirek et al., 2019; Winkowski and Kanold, 2013). However, all of these previous discoveries in tonotopic mapping are based on layer specificity. While the laminar structure is closely associated with functional projections in the AuC, they are not precisely identical. Neurons within the same layer can exhibit diversity in their molecular, morphological, physiological, and connectional features (Triarhou, 2021; Yarmohammadi et al., 2014), and therefore, categorizing cortical neurons based on their projection specificity can provide a deeper fundamental understanding of their functional organization. The A1-MGB projecting neurons play an essential role in the

86 feedforward-feedback loop of the thalamus-neocortex interplay for integrated sound
87 information processing flow (Happel et al., 2014; Happel et al., 2010) and the
88 perception of complex sounds (Clayton et al., 2021; Homma et al., 2017). However,
89 due to technical difficulties, there has been limited understanding of the functional
90 properties of these specific corticothalamic projecting neurons (Antunes and
91 Malmierca, 2021; Harris et al., 2019; Sherman and Guillery, 1998; Winer et al., 2001)
92 because they are located in deeper layers of the cortex and more difficult to be
93 accessed by means of commonly-used, single-cell-resolving recording techniques
94 such as conventional two-photon (2P) microscopy (Kobat et al., 2009; Oheim et al.,
95 2001; Takasaki et al., 2020; Tischbirek et al., 2015).

96 Recent work has established a rabies-based retrograde labeling method with
97 pathway specificity (Sun et al., 2019; Zhu et al., 2020) to circumvent the neuropil
98 contamination problem for conventional 2P imaging for CT neurons. Here, using viral
99 tracing and 2P Ca^{2+} imaging of awake head-fixed mice, we systematically revisited the
100 functional organization in the A1, specifically targeting two types of neurons with
101 projection specificity: TR (Zingg et al., 2017) and CT neurons (Gu et al., 2023), akin to
102 the input and output of the AuC. The projection specificity-based approach provides
103 detailed insight into the differences in population activity and frequency
104 response-related topographic organization between neurons with different
105 connectivity specificity.

106

107 **Results**

108 **Pathway-specific labeling of TR and CT neurons**

109 To label TR neurons, we used an anterograde trans-synaptic tracing strategy by
110 injecting a Cre-recombinase-expressing AAV in the MGB, then injecting a second AAV
111 carrying Cre-dependent GCaMP6s (AAV2/9-CaMKⅡ-DIO-GCaMP6s) in the AuC
112 (Figure 1A and B) (Zingg et al., 2017). Neurons labeled with AAV-GCaMP6s were
113 observed across all layers in AuC (Figure 1C and D). To label CT neurons, we
114 performed retrograde tracing with a rabies virus CVS-N2c-derived vector

115 (CVS-GCaMP6s) by injecting it into MGB (Figure 1E). Neurons labeled with
116 CVS-GCaMP6s were restricted to AuC L6 (Figure 1F and G) and then were imaged by
117 2P Ca^{2+} imaging, in line with our recent work (Gu et al., 2023). Whole-cell
118 patch-clamp recordings and in vivo 2P imaging showed no change in
119 electrophysiological, morphological or functional characteristics of CVS-labeled CT
120 neurons (Gu et al., 2023). To locate A1, we conducted wide-field imaging in awake
121 GCaMP6s-labeled mice, and defined that low-frequency tone (4 kHz) elicited spatially
122 restricted responses in the regions as “low-frequency (LF) area” and high-frequency
123 tone (32 kHz) elicited responses in the regions as “high-frequency (HF) area” (Figure
124 1H). In AAV-GCaMP6s labeled mice, we identified the locations of A1, anterior
125 auditory field (AAF), and secondary auditory field (A2) based on the known tonotopy
126 in mice (Figure 1H, left panel) (Issa et al., 2014; Liu et al., 2019).

127 It is worth noting that, in CVS-GCaMP6s labeled (i.e., CT neurons) mice, pure
128 tone stimulation elicited wide-field signals in only one auditory region that exhibited
129 a tonotopic gradient (Figure 1H, right panel). To identify this region in AuC, we
130 injected a retrograde tracing indicator cholera toxin subunit B conjugated with Alexa
131 555 (CTB-555) into this region, which resulted in clearly visible CTB-555 labeled cell
132 bodies in the MGBv (Figure 1I), suggesting that CVS-GCaMP6s labeled neurons were
133 located in A1(Rothschild et al., 2010). When performing 2P imaging, the average
134 power delivered to the brain was in the range of 30 - 120 mW, depending on the
135 depth of imaging. To determine whether neurons labeled with the CVS retained
136 normal response properties after deep 2P imaging, with higher laser power than
137 superficial layers imaging, we observed the broadband noise-evoked (BBN-evoked)
138 responses of these neurons over time (days) (Figure 1- figure supplementary 1A). At
139 7 and 13 days after injection, we found that CVS-labeled neurons had completely
140 normal response properties (Figure 1- figure supplementary 1B and C).

141 Next, we performed Ca^{2+} imaging of TR or CT neurons from A1 identified by
142 wide-field imaging (Figure 1J). High-titer AAV1-Cre virus has been reported to
143 anterogradely label postsynaptic neurons and also retrogradely label presynaptic
144 neurons (Zingg et al., 2017). To minimize this labeling ambiguity, we restricted the 2P

145 imaging depth of TR neurons to 200 - 400 µm, without imaging the neurons in L5 and
146 L6, which were reciprocally connected with MGB (Harris and Mrsic-Flogel, 2013).
147 These results suggest the feasibility of our approach to label and record population
148 Ca^{2+} signals with pathway specificity at single-cell resolution in awake mice.
149
150 **CT neurons exhibit no tonotopic gradient**
151 To study tonal response profiles, we delivered 330 pure tones at each focal plane (11
152 frequencies ranging from 2 - 40 kHz, 6 attenuation levels, 5 repetitions). We
153 determined the best frequency (BF) (Guo et al., 2012) of all tuned TR (Figure 2A) or
154 CT neurons (Figure 2B) at each 2P imaging focal plane. In total, we imaged 1041 TR
155 neurons in 5 animals. 46% were "tuned" neurons, 41% neurons were "irregular"
156 neurons and 13% were "silent" neurons (Figure 2- figure supplementary 2A, the
157 definitions of "irregular", "tuned" and "silent" see METHOD DETAILS). For CT neurons,
158 we imaged a total of 2721 neurons from 10 animals. 18% were "tuned" neurons, 57%
159 neurons were "irregular" neurons and 25% were "silent" neurons (Figure 2- figure
160 supplementary 2B).
161 Based on the BFs, we determined the median BF of all tuned neurons in each 2P
162 focal plane (e.g., Figure 2C and D) and related them to the position within the
163 wide-field imaging areas (Figure 2E and F), which were then used for computing the
164 tonotopic gradient. For TR neurons, we observed a clear tonotopic axis in the
165 organization of median BF ($R = 0.77$, $P < 0.001$; 2.13 octaves/mm; Figure 2G).
166 However, no such tonotopic gradient was observed in CT neurons ($R = 0.20$, $P = 0.21$;
167 0.21 octaves/mm; Figure 2H). Plotting the relative positions of all individual tuned TR
168 or CT neurons in each mouse revealed a significant low-to-high frequency gradient
169 from caudal to rostral for TR neurons ($R = 0.52$, $P < 0.001$; 1.76 octaves/mm; Figure 2I
170 and J) but an absence of tonotopy in CT neurons ($R = 0.079$, $P = 0.084$; 0.37
171 octaves/mm; Figure 2K and L). These results at single-neuron resolution confirmed
172 that TR neuronal population does possess tonotopy, as previous reports have shown
173 on a coarse scale (Kalatsky et al., 2005; Wu et al., 2006).
174 The fraction of different BF responsive neurons among TR and CT neurons

175 showed that both TR and CT neurons displayed no obvious pattern throughout A1
176 (Figure 2M). When categorized into LF or HF areas, higher proportions of TR neurons
177 responded to low-frequency sounds in the LF areas or high-frequency sounds in the
178 HF areas, whereas CT neurons showed no frequency preference in either area
179 (Figure 2N and O). Note the obvious discrepancy that the 2P imaging data here
180 shows no tonotopic gradient of L6 CT neurons, but widefield epifluorescence imaging
181 data shows a presence of tonotopic gradient from the same mice (Figure 1H), which
182 could be largely due to differences in the imaging methods and will be discussed
183 later on.
184
185 **CT neurons exhibit high heterogeneity in tuning preference**
186 Next, we performed analysis of BF spatial distribution within each focal plane.
187 Examination of BF distribution among TR or CT neurons revealed that TR neurons
188 exhibited similar frequency preference in HF or LF areas (Figure 3A), whereas CT
189 neurons displayed high heterogeneity in their frequency preferences, regardless of LF
190 or HF areas (Figure 3B).
191 To quantify the degree of BF heterogeneity, we examined BF spatial distribution
192 at the focal-plane, local, and nearest-neighboring scales. To this end, the
193 inter-quartile range of BF (IQR_{BF}, in octaves) was calculated for all tuned neurons in
194 each focal plane (Figure 3C and D). Quantitative analysis showed that CT neurons had
195 higher IQR_{BF} than TR neurons across all focal planes (Figure 3C). Similarly, evaluation
196 of LF or HF areas indicated that CT neurons had significantly higher IQR_{BF} than that of
197 TR neurons in LF areas, but showed no significant difference from TR neurons in HF
198 areas at the focal-plane level (Figure 3D).
199 To assess tone response heterogeneity at the local scale, we then calculated
200 IQR_{BF} for all tuned neurons within a 25 µm radius (Winkowski and Kanold, 2013; Zeng
201 et al., 2019) around each randomly selected CT or TR neuron (Figure 3E-G). The
202 results revealed that TR neurons also exhibited lower median IQR_{BF} than CT neurons
203 at the local scale (Figure 3F). Consistent with the focal plane scale, CT neurons had
204 significantly higher local IQR_{BF} than TR neurons in LF areas (Figure 3G). Unexpectedly,

205 the local IQR_{BF} of TR neurons in HF areas was significantly higher than that of TR
206 neurons in LF areas (Figure 3G). Further analysis across local regions revealed that
207 the local IQR_{BF} of TR neurons followed a low-to-high gradient along the
208 caudal-to-rostral axis (R = 0.2655, *P* = 0.0032; Figure 3H).

209 The analysis of Δfrequency (BF variability) (Bandyopadhyay et al., 2010; Zeng et
210 al., 2019) between nearest-neighboring TR or CT neurons was consistent with results
211 of local IQR_{BF} analysis (Figure 3I). That is, Δfrequency followed a clear gradient in the
212 organization of TR neurons along the caudal-to-rostral axis (R = 0.2463, *P* < 0.001;
213 Figure 3J). Moreover, TR neurons, but not CT neurons, displayed high IQR_{BF} in HF
214 areas compared to LF areas (Figure 3G and I). These results suggest the relative
215 heterogeneity of frequency preference among CT neurons but homogeneity among
216 TR neurons.

217

218 **Receptive field properties of TR versus CT neurons**

219 Given the above differences in the functional organization of frequency preference
220 between TR and CT neurons, we next focused our analysis on the frequency
221 responsive areas (FRAs) of individual neurons, as the FRAs directly reflect neuronal
222 auditory selectivity essential for sound processing (Sadagopan and Wang, 2008). For
223 this analysis, all tuned neurons were categorized into either a V-shaped (decreasing
224 frequency selectivity with increasing intensity), I-shaped (narrow, level-tolerant
225 tuning), or O-shaped (non-monotonic) FRA (Figure 4A and B). We found that a higher
226 proportion of CT neurons was associated with V-shaped FRAs than TR neurons,
227 whereas the proportion of CT neurons associated with I-shaped FRAs was lower than
228 that of TR neurons (Figure 4C). By contrast, no difference was detected in the
229 proportions of CT and TR neurons associated with O-shaped FRAs (Figure 4C).

230 A key feature of neuronal tuning curves is their sharpness. Common measures
231 of sharpness in V shape are half-peak bandwidth and the "quality factor" (Q), which
232 was obtained by dividing the BF of the neuron by a measure of tuning (Micheyl et al.,
233 2013), the width of the tuning curve at half-peak in this study. This analysis showed
234 that the half-peak bandwidth of CT neurons was significantly wider than that of TR

235 neurons (Figure 4D), while the Q value of CT neurons was lower than that of TR
236 neurons, especially in the HF areas (Figure 4E and F). Since higher Q values indicate
237 sharper tuning of neurons, which suggests higher frequency discrimination (Micheyl
238 et al., 2013), these results suggest that TR neurons might be responsible for finer
239 tone discrimination.

240 As the bandwidth of neurons' FRA can also reflect the selectivity of overall tonal
241 responses (Rodrigues-Dagaeff et al., 1989; Schreiner and Sutter, 1992), we examined
242 the maximum FRA width of TR or CT neurons (Figure 4G-J). BW_{max} was defined as the
243 maximum FRA width at any sound level. The quantitative analysis showed that the
244 BW_{max} of TR neurons was significantly narrower than that of CT neurons, irrespective
245 of the FRA shape (Figure 4G). In addition, the distribution of TR neurons generally
246 peaked at a BW_{max} of 1 - 2 octaves, while the distribution of CT neurons peaked at a
247 BW_{max} of 3 - 4 octaves (Figure 4H). The statistical analysis showed that CT neurons
248 had significantly higher BW_{max} than TR neurons (Figure 4I). Within LF or HF areas, TR
249 neurons had a significantly narrower BW_{max} range than CT neurons in either area.
250 Surprisingly, TR neurons in HF areas had a significantly lower BW_{max} than TR neurons
251 in LF areas (Figure 4J), suggesting that the BW_{max} distribution among TR neurons
252 might change along the caudal-to-rostral axis.

253 We then investigated the organization for intensity tuning, another crucial
254 feature in auditory perception, based on the monotonicity index (MI, see Methods
255 for details), wherein 1 indicated monotonic response increase with intensity and 0
256 indicated strong nonmonotonic tuning (de la Rocha et al., 2008; Sutter and Schreiner,
257 1995; Watkins and Barbour, 2011). The MI distribution across both TR and CT
258 neuronal populations peaked at 1 (Figure 4K). Subsequent categorization as either
259 monotonic or non-monotonic (using a criterion of MI = 0.5 (de la Rocha et al., 2008;
260 Moore and Wehr, 2013), neurons with an index < 0.5 considered intensity-tuned),
261 showed that the fraction of neurons exhibiting non-monotonic intensity response did
262 not significantly differ between TR and CT neurons (Figure 4L). However, examination
263 of MI values within LF or HF areas showed that a higher proportion of
264 non-monotonic CT neurons than TR were located in LF areas, while a larger

265 proportion of non-monotonic TR neurons were located in HF areas than in LF areas
266 (Figure 4M). In addition, among non-monotonic neurons, TR neurons had higher MI
267 than CT neurons, whereas monotonic TR neurons had a lower MI than monotonic CT
268 neurons (Figure 4N). Furthermore, we note that non-monotonic CT neurons had a
269 higher BF than monotonic CT neurons, whereas the BF was similar between
270 monotonic and non-monotonic TR neurons (Figure 4O). Finally, BW_{max} did not
271 significantly differ between monotonic and non-monotonic neurons in either the TR
272 or CT populations (Figure 4P).
273
274 **Discussion**
275 A key finding in this study is that the information flow descending from A1 to
276 thalamus via CT neurons does not preserve tonotopy, which contrasted with the
277 observation that the information flow ascending from the thalamus to A1 via TR
278 neurons exhibits clear tonotopy.
279
280 **Layer specific versus projection specific functional organization in AuC**
281 Previous studies have reported the existence of tonotopic gradients across all layers
282 of A1 including L6 (Guo et al., 2012; Tischbirek et al., 2019). CT neurons labeled with
283 CVS-GCaMP6s were restricted to AuC L6 but did not preserve tonotopy. This is
284 because only 30 - 50% of the pyramidal cells in L6 are CT neurons (Thomson, 2010),
285 and the neurons we image are restricted to MGB-projecting CT neurons, excluding CT
286 neurons projecting to other downstream nuclei (Clayton et al., 2021). Using
287 CVS-based labeling approach and 2P single-cell-resolved imaging, we successfully
288 dissected a small fraction of CT neurons from all L6 neurons and studied the
289 functional organization of this group of neurons.
290 The studies examining functional organization in AuC have mostly focused on
291 layer specificity (Bandyopadhyay et al., 2010; Montes-Lourido et al., 2021; Rothschild
292 et al., 2010; Tischbirek et al., 2019; Winkowski and Kanold, 2013), and these studies
293 have provided us with a basic understanding of the tonotopy and heterogeneity of
294 AuC. However, layer-specific representation is a relatively coarse approach.

295 Projection specificity-based approach provides detailed insight into differences in
296 population activity and frequency response-related topographic organization
297 between neurons with different connectivity specificity. For example, anatomical
298 studies of AuC in several species have identified the topographical organization of L5
299 corticocollicular projections (Bajo and Moore, 2005; Saldana et al., 1996; Stebbings
300 et al., 2014). By contrast, a recent study using a pathway-specific labeling method
301 showed that L5 corticocollicular neurons displayed a relatively weak topological
302 organization than the non-corticocollicular neurons in the same layer (Schmitt et al.,
303 2023). Those studies and our data consistently support the notion that different
304 anatomically organized projections do not necessarily transmit information with the
305 same topological alignment. Therefore, combining pathway-specific labeling and
306 in-vivo single-cell-resolved functional imaging could reveal unexpected fine-scale
307 details, and settle discrepancies arising from results obtained by individual methods
308 alone.
309
310 **CVS virus provides an effective means of mapping neuronal function in L6**
311 The CVSN2c-ΔG rabies virus strain, a recently engineered self-inactivating ΔG rabies
312 virus lacking the polymerase gene, exhibits strong neurotropism and reduced
313 cytotoxicity (Reardon et al., 2016). Previous studies have revealed that reliable neural
314 activity using the CVS-GCaMP6s virus can be maintained for at least 21 days, as
315 recorded by fiber photometry (Lin et al., 2023). In acute forebrain slices,
316 CVS-N2c-ΔG-hChR2-YFP reliably elicits action potentials in transfected cortical
317 neurons for at least 28 days after infection (Reardon et al., 2016). Our recent studies
318 also confirm that CVS-labeled CT neurons exhibit electrophysiological properties that
319 are indistinguishable from those of normal neurons (Gu et al., 2023). Here, chronic
320 2P calcium imaging shows that CT neurons retain stable sound response properties
321 for at least 13 days (Figure 1- figure supplementary 1). All of these studies suggest
322 that the CVS virus-labeling method provides an effective means of mapping neuronal
323 circuitry and manipulating neuronal activity *in vivo* in the mammalian central
324 nervous system.

325

326 **Tonotopy of CT neurons can be observed in wide-field but not 2P imaging**

327 Our 2P imaging results are not contradictory with our wide-field epifluorescence
328 imaging data (Figure 1) showing a tonotopy in A1 from the same mice that were later
329 used for 2P imaging experiments. First, the source of the fluorescence signal differs
330 between wide-field imaging and 2P imaging. Wide-field epifluorescence imaging
331 reports all fluorescent proteins from cell bodies and neuropils across layers, whereas
332 2P imaging only examines fluorescent signals from the cell bodies (Scott et al., 2018).
333 Furthermore, BF tuning from individual neurons results in a significantly closer match
334 to wide-field mapping before removal of the neuropil contribution, thus confirming
335 that the neuropil produces greater local homogeneity in BFs along with a clearer
336 global tonotopic organization (Romero et al., 2020). For L6 CT neurons, the
337 contribution of the neuropil (dendrites) is important due to the specificity of their
338 morphological structure: the cell bodies are located in L6, while their corresponding
339 apical dendrites terminate in L4 (32%) or extend to L1 (68%)(Olsen et al., 2012).

340

341 **Profiling of auditory features of "in-and-out" neurons in A1**

342 At the single-neuron level, the tonotopic organization or functional distribution of
343 adjacent neuron clusters in the AuC can be highly heterogeneous in mice (Issa et al.,
344 2014; Tao et al., 2017; Winkowski and Kanold, 2013). Our findings in this study reveal
345 that TR neurons exhibit more homogeneous functional and spatial distribution
346 (Figure 3), which contrasts with some other single-cell-resolved studies in the mouse
347 AuC (Li et al., 2017; Rothschild et al., 2010; Winkowski and Kanold, 2013). This
348 discrepancy can be also explained by the pathway specificity, i.e., only a small
349 fraction of neurons in the upper layers of AuC are thalamocortical recipients. It is
350 expected that TR neurons possess high-gradient tonotopy and sharp tuning because
351 feedforward thalamocortical projections are known to possess the same features
352 (Guo et al., 2012; Kanold et al., 2014; Winkowski and Kanold, 2013). What is
353 unexpected is that the same predictions based on the classical literature of
354 functional mapping of AuC (Guo et al., 2012; Imig et al., 1977; Recanzone et al., 1999;

355 Rothschild et al., 2010) do not apply to L6 CT neurons. This fits perfectly with a
356 previous study, which found a transition from precise, homogenous frequency
357 organization in L4 to coarse, diffuse organization in L2/3, suggesting that information
358 flow exhibits diverse selectivity after cortical processing (King et al., 2018; Winkowski
359 and Kanold, 2013).

360 What could be the functional meaning of this change in, or elimination of,
361 tonotopic organization? We suggest that descending information flow of A1-MGB
362 projection could potentially support higher cortical functions such as higher-level
363 feedback processing of complex (Homma et al., 2017; Malmierca et al., 2015) and
364 behaviorally meaningful sound (Jeschke et al., 2021; Ohl et al., 2001; Wang et al.,
365 2020; Wang et al., 2022). In addition to frequency preference, this study also
366 provides evidence illustrating the effects of cortical processing on response
367 properties. For example, BW_{max}, which reflects the degree of integration of synaptic
368 inputs from presynaptic neurons (Kratz and Manis, 2015; Li et al., 2019; Schreiner
369 and Sutter, 1992), is 3.0 octaves in CT neurons, but only 1.3 octaves in TR neurons
370 (Figure 4I), indicative of an increase in synaptic integration during cortical processing
371 (Li et al., 2019). The previous study shows that L6 CT neurons are more narrowly
372 tuned than L5 corticofugal neurons (Williamson and Polley, 2019), which is opposite
373 to what is reported here because the neurons we image are MGB-projecting CT
374 neurons. The difference in BW_{max} between TR and CT neurons is consistent with a
375 scenario in which CT neurons non-selectively "pool" inputs for higher-order feedback
376 processing of sophisticated auditory inputs that affect behavior (Wang et al., 2020;
377 Wang et al., 2022).

378

379 **Conclusion**

380 In summary, our finding fills in a knowledge gap in the auditory physiology: whereas
381 the corticothalamic feedback projection is known to contribute to higher cognitive
382 processing of behaviorally-relevant complex sounds, the basic pure-tone map that
383 underlies and facilitates these advanced processing remained unclear. Our results
384 reveal that the sensory information flow descending from the AuC to thalamus via L6

CT neurons does not arrange tonotopically. The new shift, categorizing cortical neurons based on their projection specificity, represents an advance in the conceptual framework for functional organization.

Figures

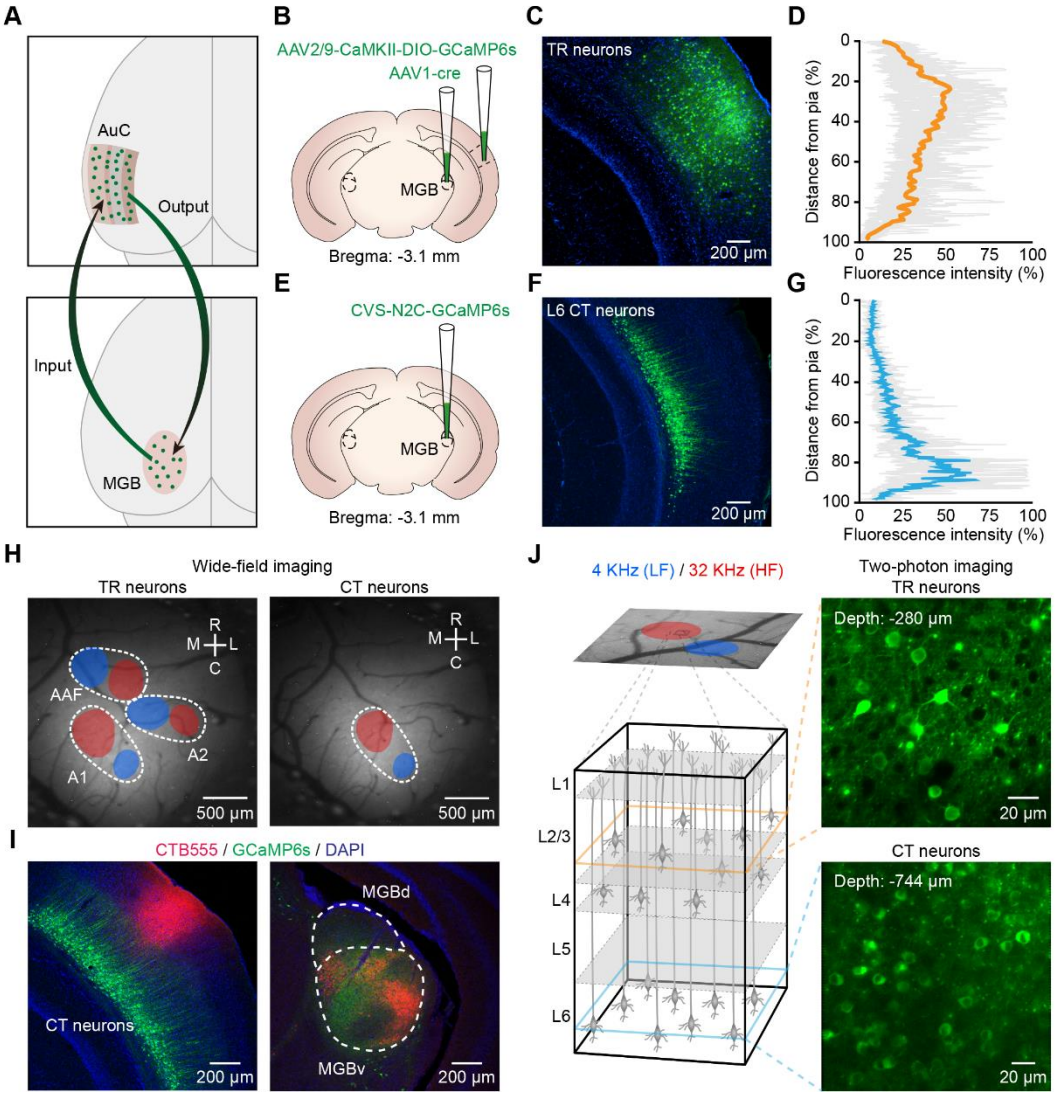

Figure 1. Imaging TR or CT neurons in A1 of awake mice. (**A**) Cartoon illustration of the auditory thalamocortical and corticothalamic circuits. (**B**) Schematic diagram of the injection site of AAV2/1-Cre in the MGB and AAV2/9-CaMKⅡ-DIO -GCaMP6s in AuC. (**C**) Coronal slice showing AAV-GCaMP6s expression in the AuC on day 21. (**D**) Fluorescence intensity of TR neurons in AuC with distance from pia (0%) to the L6/WM border (100%). (**E**) Schematic diagram of the injection site of CVS-GCaMP6s in the MGB. (**F**) Coronal slice showing the CVS-GCaMP6s retrogradely labeled neurons in the AuC on day 7. (**G**) Fluorescence intensity of CT neurons in AuC with distance from pia (0%) to the L6/WM border (100%). (**H**) Left: wide-field imaging in AAV-GCaMP6s-expressing mouse (TR neurons), fluorescence response to pure-tone stimulation with 4 kHz (blue area) and 32 kHz (red area). White dotted lines

outline the A1, A2, and AAF boundaries. Right: wide-field imaging in CVS-GCaMP6s-expressing mouse (CT neurons). (**I**) Left: a fluorescent micrograph of a coronal slice after CTB-555 loading guided by 2P imaging into A1 in a CVS-GCaMP6s-expressing mouse. Right: Micrograph of a coronal slice of the MGB from the same mouse. CTB-555 retrogradely labeled neurons were mainly concentrated in the MGBv. (**J**) Left: wide-field imaging (in a GCaMP6s-expressing mouse) in A1, fluorescence response to pure-tone stimulation with 4 kHz (low-frequency (LF) area) and 32 kHz (high-frequency (HF) area), same abbreviation for all subsequent figures. Inset panels outlined by dashed boxes show the magnified views of 2P imaging of TR or CT neurons. Right: examples of 2P images of TR and CT neurons *in vivo*, respectively.

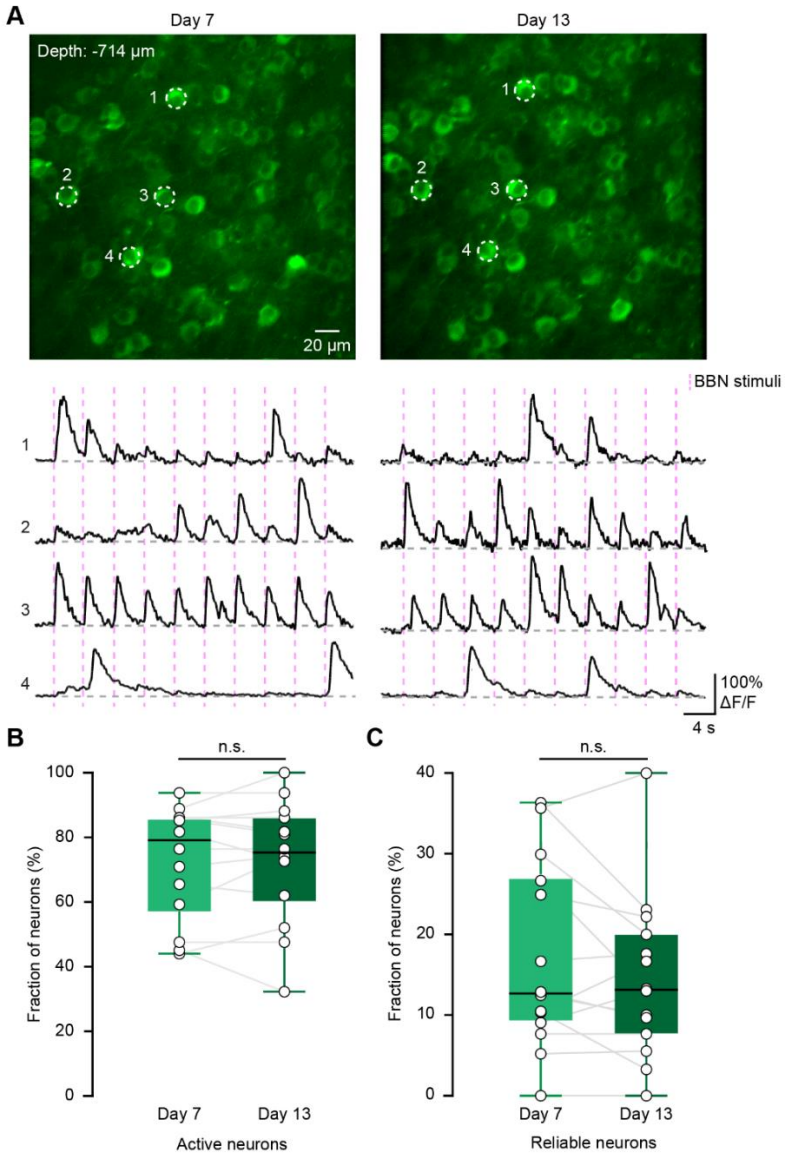

Figure 1- figure supplementary 1. Chronic *in vivo* 2P imaging of CT neurons. (**A**) Calcium imaging from L6 CT neurons in a CVS-expressing mouse, again with repeated imaging of the same focal planes on day 7 and 13 after virus injection. The dashed circle indicates the example neurons, showing fluorescence traces of neurons in the lower panel. (**B**) The comparison of the fraction of active CT neurons on day 7 and 13. *N* = 14 focal planes from 5 mice. “Day 7”: 79.14\59.26–86.11%, “Day 13”: 75.33\62.07–86.11%; P = 0.96, two-sided Wilcoxon signed-rank test, *P < 0.05, **P < 0.01, and ***P < 0.001, same statistics for boxplots. (**C**) The comparison of fraction of reliable CT neurons on day 7 and 13. “Day 7”: 12.70\9.09–26.67%, “Day 13”: 13.19\7.69–20.00%; P = 0.53. The definitions of “active” and “reliable” neurons see METHOD DETAILS.

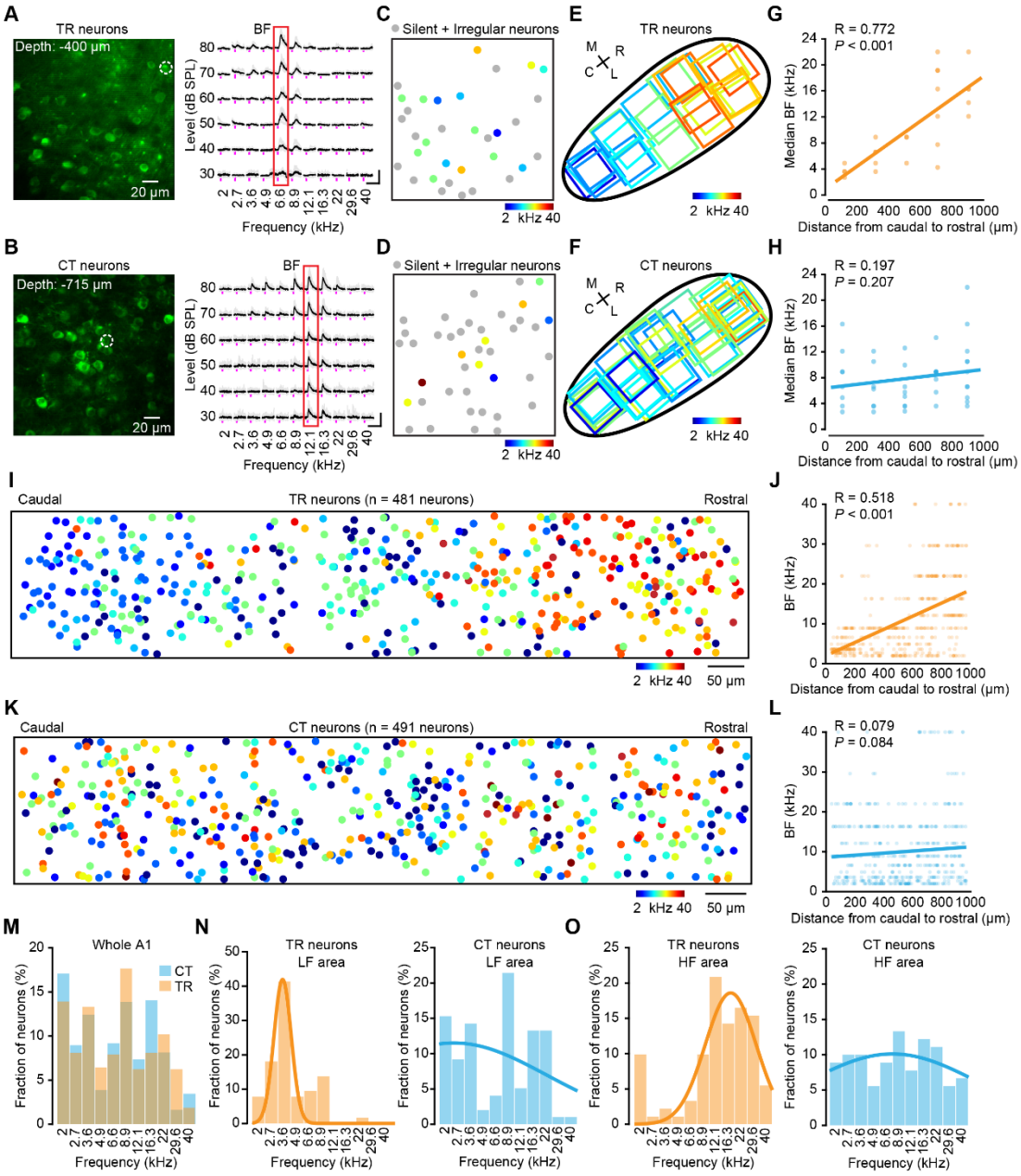

Figure 2. Tonotopic gradients of TR versus CT neurons. (**A**) Two-photon image of the focal plane used to image TR neurons in A1. The dashed circle indicates the tuned neurons. Fluorescence traces of neurons in the right panel are indicated by dashed circle ordered according to sound frequency and level. The five traces associated with the five repeats of each stimulus are plotted in gray. The average calcium signals are plotted in black. The red outline marks the BF response of the neuron. (**B**) Same as panel **A**) but for CT neurons in A1. (**C**) BF map of TR neurons. (**D**) BF map of CT neurons. (**E**) Schematic illustrating the recording locations of individual fields of view of TR neurons in A1. Outlines are color-coded according to the median BF response in the respective fields of view, with their BFs (kHz) color-coded

by the scheme below. *N* = 23 focal planes, from 5 mice. (**F**) Same as panel **E**) but for CT neurons. *N* = 40 focal planes, from 10 mice. (**G**) BF_{median} plotted against distance along the tonotopic axis for TR neurons. Scatter plots showing the correlation between the cellular BF_{median} values measured in the fields of view with 2P imaging and the corresponding extrapolated brain surface frequencies determined by wide-field imaging of TR neurons. (**H**) Same as panel **G**) but for CT neurons. (**I**) Reconstruction of the relative spatial locations of tuned TR neurons that covered the whole A1 area and color-coded according to each neuron's BF. *N* = 481 neurons from 5 mice. (**J**) Plots of TR neurons' BF and their relative distances along the caudal-to-rostral axis. (**K**) Same as panel **i** but for CT neurons. *N* = 491 neurons from 10 mice. (**L**) Same as panel **J**) but for CT neurons. (**M**) Distribution histogram of BF from all neurons in the dataset (TR: *N* = 481 neurons; CT: *N* = 491 neurons). (**N**) Distribution histogram of BF neurons that were identified in the LF area by wide-field imaging (TR: *N* = 116 neurons; CT: *N* = 98 neurons). (**O**) Distribution histogram of BF neurons that were identified in HF area by wide-field imaging (TR: *N* = 91 neurons; CT: *N* = 90 neurons).

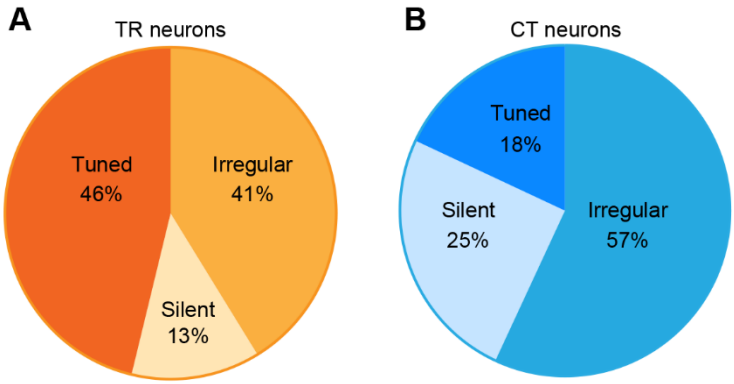

Figure 2- figure supplementary 2. Pie charts showing the percentage of responsive neurons to pure-tone stimulation of TR and CT neurons. *N* = 5 animals for TR neurons, *N* = 10 animals for CT neurons. The definitions of ''silent'' and ''irregular'' neurons see METHOD DETAILS.

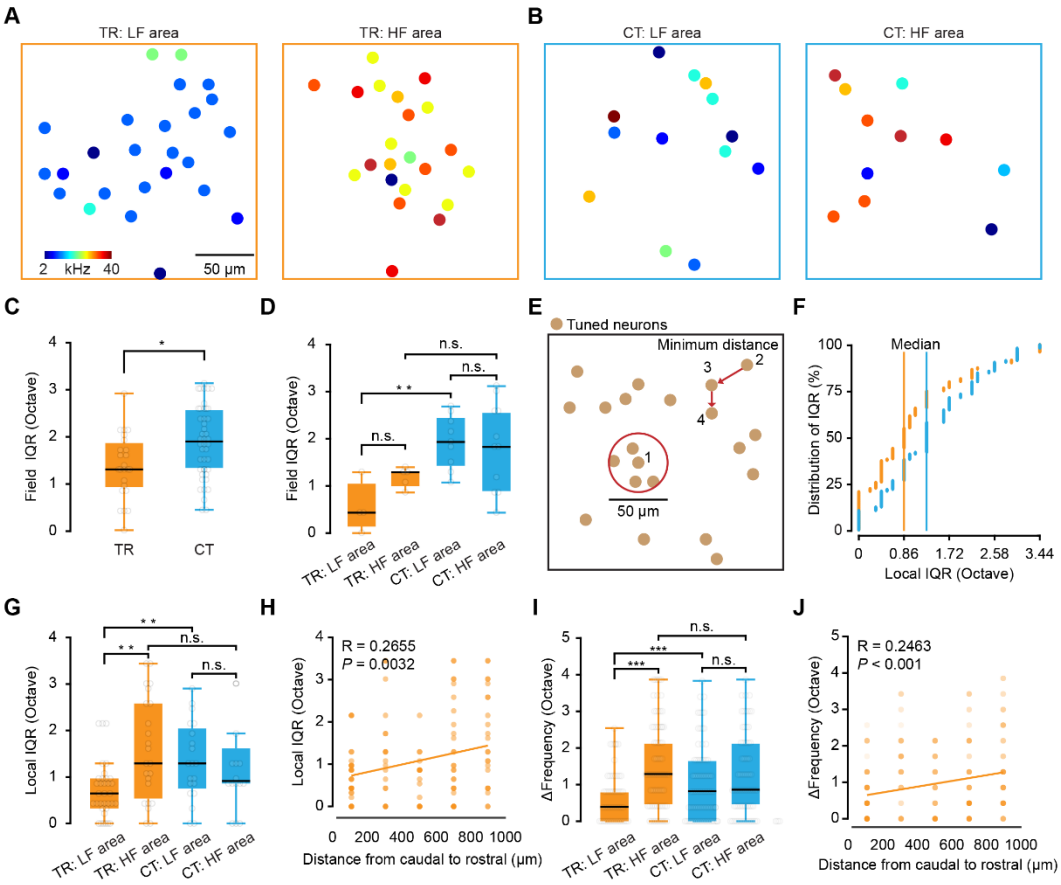

Figure 3. Heterogeneity of frequency preference in TR versus CT neurons. (**A**) Spatial distribution of all tone-selective neurons in an example imaging plane of TR neurons from LF (left) and HF (right) imaging area. (**B**) Same as panel **A**) but for CT neurons. BFs (kHz) color code is on panel **A**). (**C**) The comparison of field (200 μm) IQR of TR and CT. *N* = 23 focal planes from 5 mice for TR; *N* = 40 focal planes from 10 mice for CT. "TR": 1.29\0.91–1.88 octaves (median\25–75% percentiles, same notation for all subsequent data), "CT": 1.94\1.29–2.58 octaves. *P* = 0.016, two-sided Wilcoxon rank-sum test, **P* < 0.05, ***P* < 0.01, and ****P* < 0.001, same statistics for boxplots. (**D**) The comparison of the field IQR of TR and CT neurons in LF and HF areas. LF area: *N* = 4 focal planes from 3 mice for TR; *N* = 9 focal planes from 5 mice for CT. HF area: *N* = 5 focal planes from 5 mice for TR; *N* = 11 focal planes from 10 mice for CT. "TR: LF area": 0.43\0.22–0.86 octaves, "TR: HF area": 1.29\1.02–1.32 octaves, "CT: LF area": 1.94\1.45–2.42 octaves, "CT: HF area": 1.83\0.94–2.58 octaves. *P* (TR: LF area, HF area) = 0.11, *P* (CT: LF area, HF area) = 0.82, *P* (LF area: TR, CT) = 0.0084, *P* (HF area: TR, CT) = 0.25. (**E**) Cartoon showing how the local and minimum percentages were computed. (**F**) Cumulative percentage plot displaying local (25 μm radius) IQR around each

neuron of TR and CT. Median local IQR_{BF} of TR neurons = 0.86 octaves, *N* = 120 local planes from 5 mice; Median local IQR_{BF} of CT neurons = 1.29 octaves; *N* = 105 local planes from 10 mice. (**G**) The comparison of the local (25 µm radius) IQR of TR and CT neurons in LF and HF areas. LF area: *N* = 34 local planes for TR; *N* = 20 local planes for CT. HF area: *N* = 23 local planes for TR; *N* = 16 local planes for CT. "TR: LF area": 0.65\0.32–0.97 octaves, "TR: HF area": 1.29\0.54–2.58 octaves, "CT: LF area": 1.29\0.75–2.04 octaves, "CT: HF area": 0.91\0.86–1.61 octaves. *P* (TR: LF area, HF area) = 0.0021, *P* (CT: LF area, HF area) = 0.69, *P* (LF area: TR, CT) = 0.0057, *P* (HF area: TR, CT) = 0.34. (**H**) Local IQR_{BF} plotted against distance along the tonotopic axis for TR neurons. (**I**) The comparison of the minimum distance Δ Frequency of TR and CT neurons in LF and HF area. LF area: *N* = 116 paired neurons for TR; *N* = 87 paired neurons for CT. HF area: *N* = 91 paired neurons for TR; *N* = 78 paired neurons for CT. "TR: LF area": 0.43\0.00–0.86 octaves, "TR: HF area": 0.86\0.00–1.72 octaves, "CT: LF area": 0.43\0.00–1.29 octaves, "CT: HF area": 0.43 \0.00–1.29 octaves. *P* (TR: LF area, HF area) = 4.25e-04, *P* (CT: LF area, HF area) = 0.79, *P* (LF area: TR, CT) = 0.18, *P* (HF area: TR, CT) = 0.025. (**J**) Δ Frequency plotted against distance along the tonotopic axis for TR neurons.

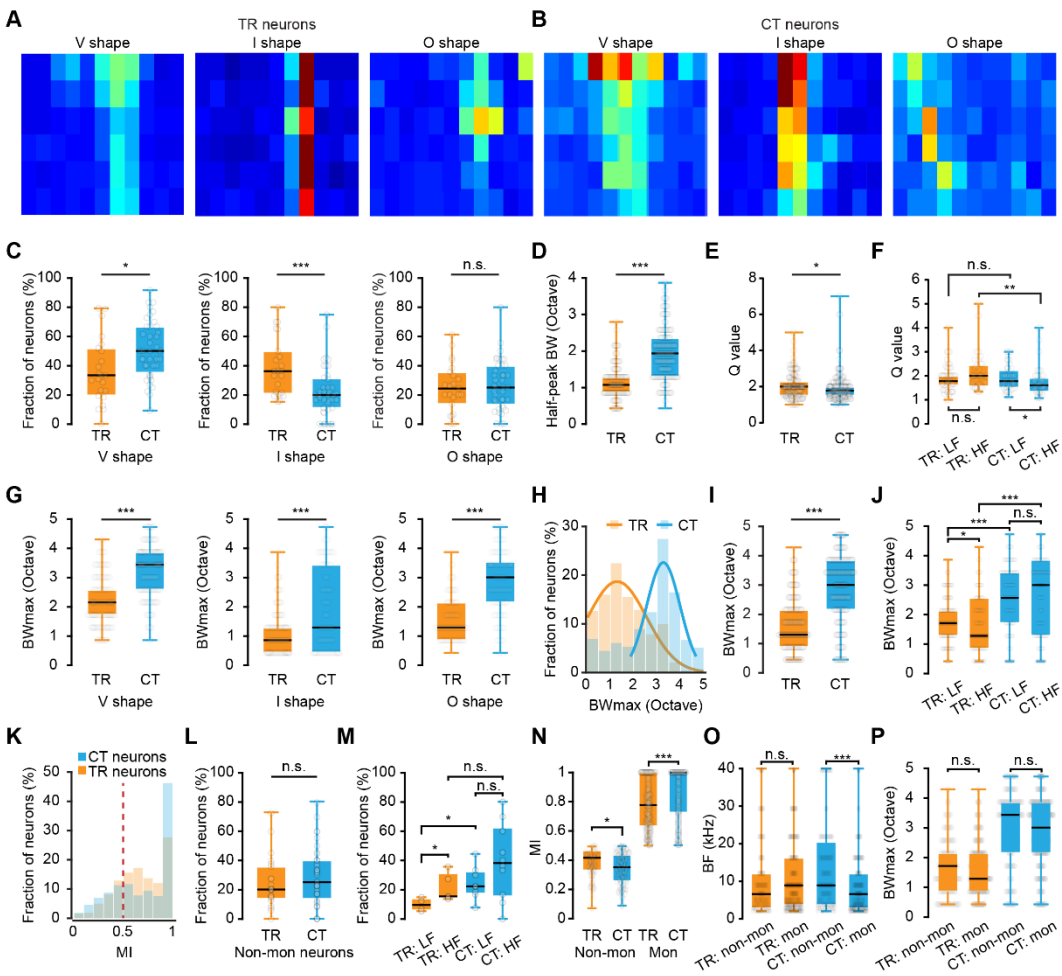

Figure 4. Receptive field properties of TR versus CT neurons. (**A**) One representative FRA from a specific type of TR neuron. Types are V shape, I shape, and O shape. See text for further details. (**B**) One representative FRA from a specific type of CT neuron. (**C**) Comparison of fraction of neurons from V, I, and O shaped neurons in TR and CT. (**D**) Comparison of half-peak bandwidth of V-shaped TR and CT neurons. *N* = 190 neurons from 5 mice for TR; *N* = 249 neurons from 10 mice for CT. "TR": 1.08\0.86–1.29 octaves, "CT": 1.94\1.29–2.37 octaves. *P* = 4.86e-29. (**E**) Comparison of Q value (bandwidth of BF/half bandwidth) of V-shaped TR and CT neurons. *N* = 190 neurons from 5 mice for TR; *N* = 249 neurons from 10 mice for CT. "TR": 2.00\1.50–2.29, "CT": 1.78\ 1.50–2.00. *P* = 0.035. (**F**) Comparison of the Q value of V-shaped TR and CT neurons in LF and HF areas. LF area: *N* = 56 neurons for TR; *N* = 49 neurons for CT. HF area: *N* = 37 neurons for TR; *N* = 41 neurons for CT. "TR: LF area": 1.78\1.60–2.00, "TR: HF area": 2.00\1.58–2.43, "CT: LF area": 1.78\1.50–2.22, "CT: HF area": 1.60\1.33–1.88. *P* (TR: LF area, HF area) = 0.20, *P* (CT: LF area, HF area) = 0.032, *P* (LF area: TR, CT) = 0.88, *P* (HF area: TR, CT) = 0.0032. (**G**) Comparison of maximum bandwidth (BW_{max})

501 from V, I, and O shaped neurons in TR and CT. V shape: *N* = 190 neurons for TR, *N* = 249
502 neurons for CT; “TR”: 2.15\1.72–2.58 octaves, “CT”: 3.44\2.58–3.87 octaves; *P* = 4.18e-29. I
503 shape: *N* = 174 neurons for TR, *N* = 112 neurons for CT; “TR”: 0.86\0.43–1.29 octaves, “CT”:
504 1.29\0.43–3.44 octaves; *P* = 4.66e-05. O shape: *N* = 117 neurons for TR, *N* = 130 neurons for
505 CT; “TR”: 1.29\0.86–2.15 octaves, “CT”: 3.01\2.15–3.44 octaves; *P* = 4.30e-19. (**H**)
506 Distribution histogram of BW_{max} from all neurons in the dataset. (**I**) Comparison of the BW_{max}
507 of TR and CT neurons. *N* = 481 neurons from 5 mice for TR, *N* = 491 neurons from 10 mice for
508 CT; “TR”: 1.29\0.86–2.15 octaves, “CT”: 3.01\2.15–3.87 octaves; *P* = 1.89e-51. (**J**)
509 Comparison of the BW_{max} of TR and CT neurons in LF and HF areas. LF area: *N* = 116 neurons
510 for TR; *N* = 98 neurons for CT. HF area: *N* = 91 neurons for TR; *N* = 90 neurons for CT. “TR: LF
511 area”: 1.72\1.29–2.15, “TR: HF area”: 1.29\ 0.86–2.47, “CT: LF area”: 2.58\ 1.72–3.44, “CT:
512 HF area”: 3.01\ 1.29–3.87. *P* (TR: LF area, HF area) = 0.034, *P* (CT: LF area, HF area) = 0.92, *P*
513 (LF area: TR, CT) = 2.44e-08, *P* (HF area: TR, CT) = 2.28e-06. (**K**) Distribution of the
514 monotonicity index (MI) of TR and CT neurons. (**L**) Comparison of the fraction of
515 non-monotonic neurons of TR and CT. *N* = 23 focal planes from 5 mice for TR, *N* = 40 focal
516 planes from 10 mice for CT; “TR”: 20.00%\12.92–31.49%, “CT”: 25.00%\14.58–40.00%; *P* =
517 0.33. (**M**) Comparison of the fraction of non-monotonic neurons of TR and CT in LF and HF
518 areas. LF area: *N* = 4 focal planes from 3 mice for TR; *N* = 9 focal planes from 5 mice for CT.
519 HF area: *N* = 5 focal planes from 5 mice for TR; *N* = 11 focal planes from 10 mice for CT. “TR:
520 LF area”: 9.55%\6.08–13.50%, “TR: HF area”: 15.38%\14.66–29.38%; “CT: LF area”:
521 22.22%\17.59–31.67%, “CT: HF area”: 38.18%\16.67–60.00%; *P* (TR: LF area, HF area) = 0.032,
522 *P* (CT: LF area, HF area) = 0.19, *P* (LF area: TR, CT) = 0.016, *P* (HF area: TR, CT) = 0.17. (**N**)
523 Comparison of the MI of non-monotonic and monotonic neurons in TR and CT. Non-mon: *N* =
524 107 neurons for TR, *N* = 128 neurons for CT; “TR”: 0.42\0.33–0.47, “CT”: 0.35\0.26–0.44; *P* =
525 7.03e-04. Mon: *N* = 374 neurons for TR, *N* = 363 neurons for CT; “TR”: 0.78\0.63–1.00, “CT”:
526 1.00\0.73–1.00; *P* = 6.19e-11. (**O**) Comparison of the BF between monotonic and
527 non-monotonic neurons in TR and CT. TR: *N* = 107 neurons for non-mon, *N* = 374 neurons for
528 mon; “non-mon”: 6.60\2.93–12.10 kHz, “mon”: 8.90\3.60–16.30 kHz; *P* = 0.69. CT: *N* = 128
529 neurons for non-mon, *N* = 363 neurons for mon; “non-mon”: 8.90\3.60–19.15 kHz, “mon”:
530 6.60\2.70–12.10 kHz; *P* = 1.64e-04. (**P**) Comparison of the BW_{max} between monotonic and

non-monotonic neurons in TR and CT. TR: *N* = 107 neurons for non-mon, *N* = 374 neurons for mon; “non-mon”: 1.72\0.86–2.15 octaves, “mon”: 1.29\0.86–2.15 octaves; *P* = 0.92. CT: *N* = 128 neurons for non-mon, *N* = 363 neurons for mon; “non-mon”: 3.44\2.15–3.87 octaves, “mon”: 3.01\2.15–3.87 octaves; *P* = 0.052.

536 # Materials and methods

537 ## Key resources table

Reagent type (species) or resource	Designation	Source or reference	Identifiers	Additional information
Genetic reagent (Mus musculus)	Mouse: C57BL/6J	Beijing HFK	RRID:IMSR_JAX:000664	https://www.jax.org/
Recombinant DNA reagent	AAV2/1-hSyn-Cre-WPRE-hGH polyA	BrainVTA	PT-0136	
Recombinant DNA reagent	AAV2/9-CaMKⅡ-DIO-GCaMP6s-WPRE-hGH pA	BrainVTA	PT-0071	
Recombinant RNA reagent	CVS-N2c-ΔG-GCaM6s	BrainCase Co., Ltd.	BC-RV-CVS715	
Peptide, recombinant protein	Alexa Fluor 555-conjugated Cholera Toxin Subunit B	Invitrogen	C34776	
Chemical compound	DAPI	Sigma-Aldrich	Cat# D9542	
Software, algorithm	Matlab	Mathworks	N/A	https://www.mathworks.com/
Software, algorithm	LabVIEW	National Instruments	N/A	https://www.ni.com/zh-cn.html
Software, algorithm	Igor Pro	Wavemetrics	N/A	https://www.wavemetrics.com/
Software, algorithm	Prism	GraphPad	N/A	https://ww

				w.graphpad.com/
Other	UHU Super Glue	DETAI	N/A	
Other	Sun Medical Super Bond C & B Kit Bonding Kit	Super-Bond	N/A	

538

539 **Animals**

540 C57BL/6J male mice (2–3 months old) were provided by the Laboratory Animal
541 Center at the Third Military Medical University. The mice were housed in a
542 temperature- and humidity-controlled room on a cycle of 12-h light/dark (lights off at
543 19:00) with free access to food and water. All animal procedures were approved by
544 the Animal Care Committee of the Third Military Medical University and were
545 performed in accordance with the principles outlined in the National Institutes of
546 Health Guide for the Care and Use of Laboratory Animals.

547

548 **Virus injections and confocal imaging**

549 Mice were anesthetized with 1% to 2% isoflurane in pure oxygen and placed in a
550 stereotactic frame (Beijing Zhongshi Dichuang Technology Development Co., Ltd.). A
551 warm heating pad was used to keep the animals at a proper body temperature
552 (36.5°C to 37.5°C). To achieve TR neurons labeling, a Cre-expressing AAV
553 (AAV2/1-hSyn-Cre-WPRE-hGH polyA, titer ≥ 1E+13vg/ml, PT-0136, BrainVTA) was
554 injected into the MGB (AP -3.1 mm, ML 2.0 mm, DV -2.8 mm from dura) and
555 DIO-expressing AAV (AAV2/9-CaMKⅡ-DIO-GCaMp6s-WPRE-hGH pA, PT-0071,
556 BrainVTA) was injected into the AuC (AP -3.1 mm, ML 3.8 mm, DV -1.4 mm from dura
557 with manipulator tilted 25° from the z-axis). For CT neuron labeling, the CVS virus
558 (CVS-N2c-ΔG-GCaM6s), packaged by BrainCase Co., Ltd., Shenzhen, China, was
559 injected into the MGB. In all the injections, approximately 100 nL of virus was
560 performed. After injection, the pipette was held in place for 10 min before retraction.

561 Tissue glue (3M Animal Care Products, Vetbond) was used for bonding the scalp
562 incision.
563 Mice were killed for histology 4 weeks after AAV injection or 7 days after CVS
564 injection. For slice preparation, mice were perfused transcardially with 4%
565 paraformaldehyde in phosphate-buffered saline. Brains were postfixed in 4%
566 paraformaldehyde overnight at 4 °C and cut into 50 µm sections on a cryostat
567 microtome (Thermo Fisher, NX50, Waltham, MA). Mounted sections were imaged on
568 a scanning confocal microscope (TCS SP5, Leica).
569
570 **Auditory stimulation**
571 Sound stimuli were delivered by an ED1 electrostatic speaker driver and a free-field
572 ES1 speaker (both from Tucker Davis Technologies). During experiments, the speaker
573 was put at a distance of ~6 cm to the left ear of the animal. The sound stimulus was
574 produced by a custom-written, LabVIEW-based program (LabVIEW 2012, National
575 Instruments) and transformed to analogue voltage through a PCI6731 card (National
576 Instruments). All the data were obtained at 1 MHz via a data acquisition device
577 (USB-6361, National Instruments) and examined by our custom-made LabVIEW
578 program. For BBN (BBN, bandwidth 0–50 kHz), the sound level was ~65 dB sound
579 pressure level (SPL). We generated a waveform segment of BBN and used the same
580 waveform segment for all experiments involving BBN.
581 For functional mapping of TR and CT neurons, sequences of randomly ordered
582 pure tones with 11 frequencies (2–40 kHz) at 6 attenuation levels (30–80 dB SPL)
583 were used. Each frequency-attenuation combination was presented 5–8 times.
584 Background noise generated by the recording hardware, especially the resonance
585 scanner of the 2P microscope, was measured to be below < 30 dB SPL for the
586 relevant frequency range. As described in our previous reports, low frequencies (<1
587 kHz) were major components of background noise. With a spectral density of ~33
588 dB/sqrt (Hz), the peak of background noise was below 1 kHz. Neither visible light nor
589 other sensory stimuli were present. The duration of a sound stimulus (tone or BBN)
590 was 100 ms.

591

592 ***In vivo* wide-field epifluorescence imaging**

593 A homemade binocular microscope (BM01, SIBET, CAS) with a 4X, 0.2 NA objective
594 (Olympus) was used to record wide-field fluorescence images in the mouse cortex for
595 establishing the reference cortical map of A1. A light-emitting diode (470 nm,
596 M470L4, Thorlabs) was used for blue illumination. Green fluorescence passed
597 through a filter cube was measured at 10 Hz with a sCMOS camera (Zyla 4.2, Andor
598 Technology). Mice injected with AAV-GCaM6s or CVS-GCaM6s were used to
599 functionally identify the region of A1. The mouse was anesthetized by isoflurane and
600 kept on a warm plate (37.5°C). A piece of bone (~5 mm × 5 mm) was removed and
601 replaced by a coverslip (3 mm in diameter). To localize A1, two pure tones (4 and 32
602 kHz) were repeatedly presented 20 times at an interval of 6 s.

603 We observed that pure tone stimulation evoked wide-field signals in only one
604 auditory region in CVS-GCaM6s mice. To confirm the region, we used the criterion
605 that the ventral part of the medial geniculate body (MGBv) is connecting with A1.
606 Injections were performed under visual guidance using 2P excitation. In the
607 experiment, we inserted the electrode into the cortical region at a depth of ~500 μm
608 below the surface. We used Alexa Fluor 555-conjugated cholera toxin subunit B (CTB)
609 as the neural tracer and injected the fluorescent CTB solution with 0.5% in phosphate
610 buffer by pressure (700 mbar) for 15min. Seven days after the fluorescent CTB
611 injection, the mice were anesthetized with pentobarbital (1.0 g/kg ip). The brain was
612 first dissected out and then it was immersed with 4% paraformaldehyde overnight.
613 To visualize fluorescent tracers, a consecutive series of coronal or horizontal sections
614 (50 μm thick) were prepared using a sliding cryotome, and then all sections were
615 mounted onto glass slides and imaged with a stereoscope (Olympus).

616

617 **Two-photon Ca^{2+} imaging in A1**

618 For 2P imaging in head-fixed awake mice, we removed the skin and muscles over the
619 right A1 after local lidocaine injection under isoflurane anesthesia (1–2%). A
620 custom-made plastic chamber (head post) designed for head-fixed mouse

experiments was then glued to the skull with cyanoacrylic glue (UHU). After recovery from surgery for 3 days, the mouse underwent head-fixation training for 3–5 days (from 1 to 4 h per day). After head-fixation training, mice gradually adapted to this posture and were able to sit comfortably for 4 h. On the recording day, a small craniotomy was performed under local anesthesia. Then the field of interest was determined by comparing the wide-field map with the blood vessel patterns to ensure A1 was imaged.

Two-photon imaging was performed with a custom-built 2P microscope system based on a 12.0 kHz resonant scanner (model “LotosScan 1.0”, Suzhou Institute of Biomedical Engineering and Technology). Two-photon excitation light was delivered by a mode-locked Ti: Sa laser (model “Mai-Tai DeepSee”, Spectra Physics), and a 40×/0.8 numerical aperture (NA) water immersion objective (Nikon) was used for imaging. For Ca^{2+} imaging experiments, the excitation wavelength was set to 920 nm. The typical size of the field of view (FOV) was ~200 µm × 200 µm. The average power delivered to the brain was in the range of 30–120 mW, depending on the depth of imaging.

Chronic 2P Ca^{2+} imaging in L6

For chronic 2P imaging, A circular cranial window (2.5 mm diameter coverslip) was implanted over the right AuC after head-post implantation. To this end, the muscle and skull fascia above the temporal skull were removed after local lidocaine (2%) injection. Afterward, a custom-made plastic chamber was fixed to the skull with dental cement (Superbond, Sun Medical Co., Ltd.) and a small craniotomy (~2.7 mm in diameter, the center point: AP: -3.0 mm, ML: -4.5 mm) was performed. The dura was removed, and the craniotomy was polished to match the size of the coverslip. A coverslip was carefully placed on top of the cortex with mild compression by tweezers. The coverslip was sealed with UV-curing dental cement (Tetric N-flow, Ivoclar Co., Ltd.). Antibiotics (Cefazolin, 500 mg/kg, North China Pharmaceutical Group Corporation) were administered before surgery, as well as until 3 days after surgery. 3 days of post-surgery recovery were needed before head-fixation training.

651 Continuous 2P Ca^{2+} imaging was performed on day 7 and 13. To minimize the
652 bleaching of cells, we used low laser illumination in the deep imaging, based on
653 high-quality imaging of CT neurons with CVS labeling strategy. The repeated imaging
654 FOVs were identified on consecutive days based on superficial blood vessels and
655 nearby blood vessels, then further refined by visually matching reference images
656 acquired from precedent days.
657
658 **QUANTIFICATION AND STATISTICAL ANALYSIS**
659 Data were analyzed using custom-written software in LabVIEW 2012 (National
660 Instruments), Igor Pro 5.0 (Wavemetrics), Image 1.51 (NIH), Prism 8.4 (GraphPad)
661 and MATLAB 2014a (MathWorks).
662
663 **Wide-field imaging data analysis**
664 In each mouse, the recorded cortical images were first down sampled from the
665 original 750 × 1200 pixels to 75 × 120 pixels. After that, the frames recorded with
666 sound stimuli were averaged across 20 trials. To enhance the signal-to-noise ratio,
667 spatial averaging was conducted over 5 × 5 pixels by a matrix filter, and temporal
668 averaging was conducted with three consecutive images. The pre-processed images
669 were then temporally normalized to obtain the relative changes in fluorescence (f)
670 pixel-by-pixel. With the baseline fluorescence (f0) obtained by averaging the images
671 of 800 ms before sound stimulation, the relative fluorescence changes of each pixel
672 were calculated as $\Delta f/f = (f - f0)/f0$. The normalized images are shown on a
673 color-coded scale to visualize the relative fluorescence changes ($\Delta f/f$) in the cortex.
674
675 **Two-photon imaging data analysis**
676 To correct motion-related artifacts in imaging data, a frame-by-frame alignment
677 algorithm was used to minimize the sum of squared intensity differences between
678 each frame image and a template, which was the average of the selected image
679 frames. To extract fluorescence signals, neurons were visually identified, and drawing
680 regions of interest (ROIs) based on fluorescence intensity was performed.

681 Fluorescence changes (f) were calculated by averaging the corresponding pixel values
682 for each ROI. Relative fluorescence changes Δf/f = (f−f0)/f0 were calculated as Ca^{2+}
683 signals, where the baseline fluorescence f0 was estimated as the 25th percentile of
684 the entire fluorescence recording. To calculate the amplitude of sound-evoked Ca^{2+}
685 transients, we performed automatic Ca^{2+} transient detection based on threshold
686 criteria regarding peak amplitude and rising rate. The noise level was set to be 3
687 times the standard deviation of the baseline (window length: 1 s). The peak
688 amplitude and the rate of rising of the Ca^{2+} signals were calculated to determine
689 whether it was a true transient. The trace of the detected Ca^{2+} transient was first
690 extracted by exponential infinite impulse response (IIR) filtering (window length: 200
691 ms) and then subtracted from the original signal. The residual fluorescence trace was
692 used as the baseline for the next transient detection, similar to previously published
693 peeling approaches.
694
695 **Sound-evoked Ca^{2+} responsiveness**
696 **BBN-evoked Ca^{2+} responsiveness**
697 For data from chronic Ca^{2+} imaging, we tracked the same FOV based on the last
698 training day. We removed the outer ∼10% of the image from each ROI to account for
699 edge effects or imaging deviation. The success rate was defined as the fraction of
700 sound-evoked responses during 10 consecutive BBN stimuli. Note that "Active"
701 neurons showed clear Ca^{2+} transients during the entire recording duration, including
702 spontaneous and BBN-evoked responses. The neurons with a success rate ≥ 50%
703 were defined as "Reliable" neurons among active neurons.
704
705 **Pure tone-evoked Ca^{2+} responsiveness**
706 The frequency response area (FRA) of each ROI was constructed from the 55 average
707 responses to all of the unique frequency-attenuation combinations. The frequency
708 tuning curves were constructed by plotting the average values (and the s.e.m.) of the
709 calcium signal amplitudes from single trials for each frequency tested. If more than
710 one area of contiguous frequency-level combinations remained, the largest one was

711 defined as the FRA. The amplitude of a Ca^{2+} signal was determined as the average
712 value for a period of 200 ms around the peak of the calcium transient. The baseline
713 value was calculated for a period of 100 ms before the onset of the auditory stimulus.
714 Pure tone frequencies that induced response amplitudes higher than half of the
715 maximal response were defined as effective frequencies.

716 "Irregular" neurons exhibited spontaneous activity with highly variable
717 responses to sound stimulation. "Tuned" neurons were responsive neurons that
718 demonstrated significant selectivity for certain stimuli. "Silent" neurons were defined
719 as those that remained completely inactive during our recording period (> 30 min).
720 For tuned neurons, the best frequency (BF) was defined as the sound frequency
721 associated with the highest response averaged across all sound levels. FRAs showing
722 decreasing frequency selectivity with increasing intensity were classified as being V
723 shape, constant frequency selectivity with increasing intensity was classified as being
724 I shape, responsiveness to a small range of intensities and frequencies was classified
725 as being O shape if the peak response was not to the highest intensity. Maximum
726 bandwidth (BW_{max}) was defined as the maximum FRA width at any level.

727 To compare the BF heterogeneity, we analyzed the BF distribution in fixed-size
728 analysis windows. The BF heterogeneity was quantified by the interquartile range
729 (IQR) of the distribution. For filed IQR, if less than 5 neurons were within a 100 µm
730 radius (including the center neuron), no IQR was calculated(Schmitt et al., 2023). For
731 Large-scale analysis, imaging regions in separate mice were aligned with each other
732 according to the caudal-to-rostral gradient that was identifiable in the wide-field
733 images.

734 The monotonicity index (MI) characterizes the strength of a neuron's intensity
735 tuning. We defined MI as the neuron's response at maximum intensity (80 dB)
736 divided by its maximum response(Moore and Wehr, 2013; Sutter and Schreiner,
737 1995). An MI of 1 indicates no intensity tuning; an MI near zero indicates very strong
738 intensity tuning.

739

740 **Statistics**

To compare data between groups, we used the nonparametric Wilcoxon rank sum test (unpaired), and Wilcoxon signed-rank test (paired) to determine statistical significance ($P < 0.05$) between them. In the text, summarized data are presented as the median\25th–75th percentiles. In the figures, the data presented in the box-and-whisker plot indicate the median (center line), 25th and 75th percentiles (Q1 and Q3), i.e., IQR (box), Q1-1.5 × IQR and Q3 + 1.5 × IQR (whiskers), and all other data with error bars are presented as the mean ± s.e.m.

Acknowledgments

The authors would like to thank Jia Lou for the cartoon art and figure layout. This work was supported by grants from the National Key R&D Program of China (2021YFA0805000), the National Natural Science Foundation of China (31925018, 32127801, 32300937, T2241002), the Jiangsu Provincial Big Science Facility Initiative (BM2022010), and Guangxi Science and Technology Base & Talents Fund (GUIKE AD22035948). X.C. is a member of the CAS Center for Excellence in Brain Science and Intelligence Technology.

Additional information

Funding

Funder	Grant reference number	Author
National Key R&D Program of China	2021YFA0805000	Xiaowei Chen
National Natural Science Foundation of China	31925018	Xiaowei Chen
National Natural Science Foundation of China	32127801	Xiaowei Chen
National Natural Science Foundation of China	32300937	Jianxiong Zhang
National Natural Science Foundation of China	T2241002	Jianxiong Zhang
Jiangsu Provincial Big Science Facility Initiative	BM2022010	Hongbo Jia

Guangxi Science and Technology Base & Talents Fund GUIKE AD22035948 Xiaowei Chen

Author contributions

X.C. and H.J. conceived the project. X.C., JX.Z. and Y.Z. designed the experiments. M.G. performed the experiments with the help of R.L., K.L., X.W. and JH.Z.; X.C., H.J., Y.Z., S.L., JX.Z., and M.G. devised the data analysis methods; M.G., S.L., Yun.Z., X.L., C.Z. and JX.Z. performed the data analysis; JX.Z., H.J., Y.Z. and X.C. inspected the data and evaluated the findings; M.G., JX.Z., Y.Z., F.O., X.C. and H.J. wrote the manuscript with the help from all authors.

Author ORCIDs

Xiaowei Chen: https://orcid.org/0000-0003-0906-6666
Jianxiong Zhang: https://orcid.org/0000-0003-2245-8752
Yi Zhou: https://orcid.org/0000-0002-2623-8960

Ethics

All experiments were approved by the Animal Care Committee of the Third Military Medical University (Approval number: AMUWEC20230061).

Additional files

Data availability

Wide-field imaging and two-photon imaging are available upon request from the corresponding author. Source data underlying Figs. 2–4 is available as a Source data file. No datasets that require mandatory deposition into a public database were generated during the current study. Source data are provided in this paper.

Code availability

The codes supporting the current study have not been deposited in a public

repository, but are available from the corresponding author upon request.

References

Andersen RA, Knight PL, Merzenich MM. 1980. The thalamocortical and corticothalamic connections of AI, AII, and the anterior auditory field (AAF) in the cat: evidence for two largely segregated systems of connections. *Journal of Comparative Neurology* 194: 663-701. DIO: https://doi.org/10.1002/cne.901940312, PMID: 7451688

Antunes FM, Malmierca MS. 2021. Corticothalamic Pathways in Auditory Processing: Recent Advances and Insights From Other Sensory Systems. *Front Neural Circuits* 15: 721186. DIO: https://doi.org/10.3389/fncir.2021.721186, PMID: 34489648

Bajo VM, Moore DR. 2005. Descending projections from the auditory cortex to the inferior colliculus in the gerbil, Meriones unguiculatus. *Journal of Comparative Neurology* 486: 101-16. DIO: https://doi.org/10.1002/cne.20542, PMID: 15844210

Bandyopadhyay S, Shamma SA, Kanold PO. 2010. Dichotomy of functional organization in the mouse auditory cortex. *Nat Neurosci* 13: 361-8. DIO: https://doi.org/10.1038/nn.2490, PMID: 20118924

Bizley JK, Nodal FR, Nelken I, King AJ. 2005. Functional organization of ferret auditory cortex. *Cerebral Cortex* 15: 1637-53. DIO: https://doi.org/10.1093/cercor/bhi042, PMID: 15703254

Budinger E, Heil P, Scheich H. 2000. Functional organization of auditory cortex in the Mongolian gerbil (Meriones unguiculatus). IV. Connections with anatomically characterized subcortical structures. *European Journal of Neuroscience* 12: 2452-74. DIO: https://doi.org/10.1046/j.1460-9568.2000.00143.x, PMID: 10947822

Clayton KK, Williamson RS, Hancock KE, Tasaka GI, Mizrahi A, Hackett TA, Polley DB. 2021. Auditory Corticothalamic Neurons Are Recruited by Motor Preparatory Inputs. *Current Biology* 31: 310-321 e5. DIO: https://doi.org/10.1016/j.cub.2020.10.027, PMID: 33157020

Clopton BM, Winfield JA, Flammino FJ. 1974. Tonotopic organization: review and analysis. *Brain Research* 76: 1-20. DIO: https://doi.org/10.1016/0006-8993(74)90509-5, PMID: 4367399

Constantinople CM, Bruno RM. 2013. Deep cortical layers are activated directly by thalamus. *Science* 340: 1591-4. DIO: https://doi.org/10.1126/science.1236425, PMID: 23812718

de la Rocha J, Marchetti C, Schiff M, Reyes AD. 2008. Linking the response properties of cells in auditory cortex with network architecture: cotuning versus lateral inhibition. *Journal of Neuroscience* 28: 9151-63. DIO: https://doi.org/10.1523/JNEUROSCI.1789-08.2008, PMID: 18784296

Gu M, Li X, Liang S, Zhu J, Sun P, He Y, Yu H, Li R, Zhou Z, Lyu J, Li SC, Budinger E, Zhou Y, Jia H, Zhang J, Chen X. 2023. Rabies virus-based labeling of layer 6 corticothalamic neurons for two-photon imaging in vivo. *iScience* 26: 106625. DIO: https://doi.org/10.1016/j.isci.2023.106625, PMID: 37250327

Guo W, Chambers AR, Darrow KN, Hancock KE, Shinn-Cunningham BG, Polley DB. 2012. Robustness of cortical topography across fields, laminae, anesthetic states, and neurophysiological signal types. *Journal of Neuroscience* 32: 9159-72. DIO: https://doi.org/10.1523/JNEUROSCI.0065-12.2012, PMID: 22764225

Hackett TA, Stepniewska I, Kaas JH. 1998. Subdivisions of auditory cortex and ipsilateral cortical connections of the parabelt auditory cortex in macaque monkeys. *Journal of Comparative Neurology* 394: 475-95. DIO: https://doi.org/10.1002/(sici)1096-9861(19980518)394:4<475::aid-cne6>3.0.co;2-z, PMID: 9590556

Happel MF, Deliano M, Handschuh J, Ohl FW. 2014. Dopamine-modulated recurrent corticoefferent

feedback in primary sensory cortex promotes detection of behaviorally relevant stimuli. *Journal of Neuroscience* 34: 1234-47. DIO: https://doi.org/10.1523/JNEUROSCI.1990-13.2014, PMID: 24453315

Happel MF, Jeschke M, Ohl FW. 2010. Spectral integration in primary auditory cortex attributable to temporally precise convergence of thalamocortical and intracortical input. *Journal of Neuroscience* 30: 11114-27. DIO: https://doi.org/10.1523/JNEUROSCI.0689-10.2010, PMID: 20720119

Harris JA, Mihalas S, Hirokawa KE, Whitesell JD, Choi H, Bernard A, Bohn P, Caldejon S, Casal L, Cho A, Feiner A, Feng D, Gaudreault N, Gerfen CR, Graddis N, Groblewski PA, Henry AM, Ho A, Howard R, Knox JE, Kuan L, Kuang X, Lecoq J, Lesnar P, Li Y, Luviano J, McConoughey S, Mortrud MT, Naeemi M, Ng L, Oh SW, Ouellette B, Shen E, Sorensen SA, Wakeman W, Wang Q, Wang Y, Williford A, Phillips JW, Jones AR, Koch C, Zeng H. 2019. Hierarchical organization of cortical and thalamic connectivity. *Nature* 575: 195-202. DIO: https://doi.org/10.1038/s41586-019-1716-z, PMID: 31666704

Harris KD, Mrsic-Flogel TD. 2013. Cortical connectivity and sensory coding. *Nature* 503: 51-8. DIO: https://doi.org/10.1038/nature12654, PMID: 24201278

Homma NY, Bajo VM. 2021. Lemniscal Corticothalamic Feedback in Auditory Scene Analysis. *Frontiers in Neuroscience* 15: 723893. DIO: https://doi.org/10.3389/fnins.2021.723893, PMID: 34489635

Homma NY, Happel MFK, Nodal FR, Ohl FW, King AJ, Bajo VM. 2017. A Role for Auditory Corticothalamic Feedback in the Perception of Complex Sounds. *Journal of Neuroscience* 37: 6149-6161. DIO: https://doi.org/10.1523/JNEUROSCI.0397-17.2017, PMID: 28559384

Humphries C, Liebenthal E, Binder JR. 2010. Tonotopic organization of human auditory cortex. *Neuroimage* 50: 1202-11. DIO: https://doi.org/10.1016/j.neuroimage.2010.01.046, PMID: 20096790

Imig TJ, Ruggero MA, Kitzes LM, Javel E, Brugge JF. 1977. Organization of auditory cortex in the owl monkey (Aotus trivirgatus). *Journal of Comparative Neurology* 171: 111-28. DIO: https://doi.org/10.1002/cne.901710108, PMID: 401509

Issa JB, Haeffele BD, Agarwal A, Bergles DE, Young ED, Yue DT. 2014. Multiscale optical Ca2+ imaging of tonal organization in mouse auditory cortex. *Neuron* 83: 944-59. DIO: https://doi.org/10.1016/j.neuron.2014.07.009, PMID: 25088366

Jasmin K, Lima CF, Scott SK. 2019. Understanding rostral-caudal auditory cortex contributions to auditory perception. *Nature Reviews Neuroscience* 20: 425-434. DIO: https://doi.org/10.1038/s41583-019-0160-2, PMID: 30918365

Jeschke M, Ohl FW, Wang X. 2021. Effects of Cortical Cooling on Sound Processing in Auditory Cortex and Thalamus of Awake Marmosets. *Front Neural Circuits* 15: 786740. DIO: https://doi.org/10.3389/fncir.2021.786740, PMID: 35069125

Jones EG. 2001. The thalamic matrix and thalamocortical synchrony. *Trends in Neurosciences* 24: 595-601. DIO: https://doi.org/10.1016/s0166-2236(00)01922-6, PMID: 11576674

Kajikawa Y, de La Mothe L, Blumell S, Hackett TA. 2005. A comparison of neuron response properties in areas A1 and CM of the marmoset monkey auditory cortex: tones and broadband noise. *Journal of Neurophysiology* 93: 22-34. DIO: https://doi.org/10.1152/jn.00248.2004, PMID: 15342713

Kalatsky VA, Polley DB, Merzenich MM, Schreiner CE, Stryker MP. 2005. Fine functional organization of auditory cortex revealed by Fourier optical imaging. *Proceedings of the National Academy of Sciences of the United States of America* 102: 13325-30. DIO: https://doi.org/10.1073/pnas.0505592102, PMID: 16141342

Kanold PO, Nelken I, Polley DB. 2014. Local versus global scales of organization in auditory cortex. *Trends in Neurosciences* 37: 502-10. DIO: https://doi.org/10.1016/j.tins.2014.06.003, PMID: 25002236

King AJ, Teki S, Willmore BDB. 2018. Recent advances in understanding the auditory cortex. *F1000Res*

7 DIO: https://doi.org/10.12688/f1000research.15580.1, PMID: 30345008

Kirchgessner MA, Franklin AD, Callaway EM. 2020. Context-dependent and dynamic functional influence of corticothalamic pathways to first- and higher-order visual thalamus. *Proceedings of the National Academy of Sciences of the United States of America* 117: 13066-13077. DIO: https://doi.org/10.1073/pnas.2002080117, PMID: 32461374

Kobat D, Durst ME, Nishimura N, Wong AW, Schaffer CB, Xu C. 2009. Deep tissue multiphoton microscopy using longer wavelength excitation. *Optics Express* 17: 13354-13364. DIO: https://doi.org/10.1364/Oe.17.013354, PMID: WOS:000268843700009

Kratz MB, Manis PB. 2015. Spatial organization of excitatory synaptic inputs to layer 4 neurons in mouse primary auditory cortex. *Front Neural Circuits* 9: 17. DIO: https://doi.org/10.3389/fncir.2015.00017, PMID: 25972787

Lee CC. 2013. Thalamic and cortical pathways supporting auditory processing. *Brain and Language* 126: 22-8. DIO: https://doi.org/10.1016/j.bandl.2012.05.004, PMID: 22728130

Lee CC, Schreiner CE, Imaizumi K, Winer JA. 2004. Tonotopic and heterotopic projection systems in physiologically defined auditory cortex. *Neuroscience* 128: 871-87. DIO: https://doi.org/10.1016/j.neuroscience.2004.06.062, PMID: 15464293

Lee CC, Winer JA. 2005. Principles governing auditory cortex connections. *Cerebral Cortex* 15: 1804-14. DIO: https://doi.org/10.1093/cercor/bhi057, PMID: 15800026

Li H, Liang F, Zhong W, Yan L, Mesik L, Xiao Z, Tao HW, Zhang LI. 2019. Synaptic Mechanisms for Bandwidth Tuning in Awake Mouse Primary Auditory Cortex. *Cerebral Cortex* 29: 2998-3009. DIO: https://doi.org/10.1093/cercor/bhy165, PMID: 30010857

Li J, Zhang J, Wang M, Pan J, Chen X, Liao X. 2017. Functional imaging of neuronal activity of auditory cortex by using Cal-520 in anesthetized and awake mice. *Biomed Opt Express* 8: 2599-2610. DIO: https://doi.org/10.1364/boe.8.002599, PMID: 28663893

Lin KZ, Li L, Ma WY, Yang X, Han ZP, Luo NS, Wang J, Xu FQ. 2023. A rabies virus-based toolkit for efficient retrograde labeling and monosynaptic tracing. *Neural Regen Res* 18: 1827-1833. DIO: https://doi.org/10.4103/1673-5374.358618, PMID: 36751812

Liu J, Whiteway MR, Sheikhattar A, Butts DA, Babadi B, Kanold PO. 2019. Parallel Processing of Sound Dynamics across Mouse Auditory Cortex via Spatially Patterned Thalamic Inputs and Distinct Areal Intracortical Circuits. *Cell Rep* 27: 872-885 e7. DIO: https://doi.org/10.1016/j.celrep.2019.03.069, PMID: 30995483

Malmierca MS, Anderson LA, Antunes FM. 2015. The cortical modulation of stimulus-specific adaptation in the auditory midbrain and thalamus: a potential neuronal correlate for predictive coding. *Front Syst Neurosci* 9: 19. DIO: https://doi.org/10.3389/fnsys.2015.00019, PMID: 25805974

Merzenich MM, Brugge JF. 1973. Representation of the cochlear partition of the superior temporal plane of the macaque monkey. *Brain Research* 50: 275-96. DIO: https://doi.org/10.1016/0006-8993(73)90731-2, PMID: 4196192

Merzenich MM, Kaas JH, Roth GL. 1976. Auditory cortex in the grey squirrel: tonotopic organization and architectonic fields. *Journal of Comparative Neurology* 166: 387-401. DIO: https://doi.org/10.1002/cne.901660402, PMID: 1270613

Micheyl C, Schrater PR, Oxenham AJ. 2013. Auditory frequency and intensity discrimination explained using a cortical population rate code. *PLoS Computational Biology* 9: e1003336. DIO: https://doi.org/10.1371/journal.pcbi.1003336, PMID: 24244142

Montes-Lourido P, Kar M, David SV, Sadagopan S. 2021. Neuronal selectivity to complex vocalization

features emerges in the superficial layers of primary auditory cortex. *PLoS Biology* 19: e3001299. DIO: https://doi.org/10.1371/journal.pbio.3001299, PMID: 34133413

Moore AK, Wehr M. 2013. Parvalbumin-expressing inhibitory interneurons in auditory cortex are well-tuned for frequency. *Journal of Neuroscience* 33: 13713-23. DIO: https://doi.org/10.1523/JNEUROSCI.0663-13.2013, PMID: 23966693

Morel A, Garraghty PE, Kaas JH. 1993. Tonotopic organization, architectonic fields, and connections of auditory cortex in macaque monkeys. *Journal of Comparative Neurology* 335: 437-59. DIO: https://doi.org/10.1002/cne.903350312, PMID: 7693772

Nelken I, Bizley JK, Nodal FR, Ahmed B, Schnupp JW, King AJ. 2004. Large-scale organization of ferret auditory cortex revealed using continuous acquisition of intrinsic optical signals. *Journal of Neurophysiology* 92: 2574-88. DIO: https://doi.org/10.1152/jn.00276.2004, PMID: 15152018

Norman-Haignere S, Kanwisher NG, McDermott JH. 2015. Distinct Cortical Pathways for Music and Speech Revealed by Hypothesis-Free Voxel Decomposition. *Neuron* 88: 1281-1296. DIO: https://doi.org/10.1016/j.neuron.2015.11.035, PMID: 26687225

Oheim M, Beaurepaire E, Chaigneau E, Mertz J, Charpak S. 2001. Two-photon microscopy in brain tissue: parameters influencing the imaging depth. *Journal of Neuroscience Methods* 111: 29-37. DIO: https://doi.org/10.1016/s0165-0270(01)00438-1, PMID: 11574117

Ohga S, Tsukano H, Horie M, Terashima H, Nishio N, Kubota Y, Takahashi K, Hishida R, Takebayashi H, Shibuki K. 2017. DIO: https://doi.org/10.1101/226100,

Ohl FW, Scheich H, Freeman WJ. 2000. Topographic analysis of epidural pure-tone-evoked potentials in gerbil auditory cortex. *Journal of Neurophysiology* 83: 3123-32. DIO: https://doi.org/10.1152/jn.2000.83.5.3123, PMID: 10805706

Ohl FW, Scheich H, Freeman WJ. 2001. Change in pattern of ongoing cortical activity with auditory category learning. *Nature* 412: 733-6. DIO: https://doi.org/10.1038/35089076, PMID: 11507640

Olsen SR, Bortone DS, Adesnik H, Scanziani M. 2012. Gain control by layer six in cortical circuits of vision. *Nature* 483: 47-52. DIO: https://doi.org/10.1038/nature10835, PMID: 22367547

Pardi MB, Vogenstahl J, Dalmay T, Spano T, Pu DL, Naumann LB, Kretschmer F, Sprekeler H, Letzkus JJ. 2020. A thalamocortical top-down circuit for associative memory. *Science* 370: 844-848. DIO: https://doi.org/10.1126/science.abc2399, PMID: 33184213

Petreanu L, Mao T, Sternson SM, Svoboda K. 2009. The subcellular organization of neocortical excitatory connections. *Nature* 457: 1142-5. DIO: https://doi.org/10.1038/nature07709, PMID: 19151697

Polley DB, Read HL, Storace DA, Merzenich MM. 2007. Multiparametric auditory receptive field organization across five cortical fields in the albino rat. *Journal of Neurophysiology* 97: 3621-38. DIO: https://doi.org/10.1152/jn.01298.2006, PMID: 17376842

Reale RA, Imig TJ. 1980. Tonotopic organization in auditory cortex of the cat. *Journal of Comparative Neurology* 192: 265-91. DIO: https://doi.org/10.1002/cne.901920207, PMID: 7400399

Reardon TR, Murray AJ, Turi GF, Wirblich C, Croce KR, Schnell MJ, Jessell TM, Losonczy A. 2016. Rabies Virus CVS-N2c(DeltaG) Strain Enhances Retrograde Synaptic Transfer and Neuronal Viability. *Neuron* 89: 711-24. DIO: https://doi.org/10.1016/j.neuron.2016.01.004, PMID: 26804990

Recanzone GH, Schreiner CE, Sutter ML, Beitel RE, Merzenich MM. 1999. Functional organization of spectral receptive fields in the primary auditory cortex of the owl monkey. *Journal of Comparative Neurology* 415: 460-81. DIO: https://doi.org/10.1002/(sici)1096-9861(19991227)415:4<460::aid-cne4>3.0.co;2-f, PMID: 10570456

Rodrigues-Dagaeff C, Simm G, De Ribaupierre Y, Villa A, De Ribaupierre F, Rouiller EM. 1989. Functional organization of the ventral division of the medial geniculate body of the cat: evidence for a rostro-caudal gradient of response properties and cortical projections. *Hearing Research* 39: 103-25. DIO: https://doi.org/10.1016/0378-5955(89)90085-3, PMID: 2737959

Romero S, Hight AE, Clayton KK, Resnik J, Williamson RS, Hancock KE, Polley DB. 2020. Cellular and Widefield Imaging of Sound Frequency Organization in Primary and Higher Order Fields of the Mouse Auditory Cortex. *Cerebral Cortex* 30: 1603-1622. DIO: https://doi.org/10.1093/cercor/bhz190, PMID: 31667491

Rothschild G, Nelken I, Mizrahi A. 2010. Functional organization and population dynamics in the mouse primary auditory cortex. *Nat Neurosci* 13: 353-60. DIO: https://doi.org/10.1038/nn.2484, PMID: 20118927

Sadagopan S, Wang X. 2008. Level invariant representation of sounds by populations of neurons in primary auditory cortex. *Journal of Neuroscience* 28: 3415-26. DIO: https://doi.org/10.1523/JNEUROSCI.2743-07.2008, PMID: 18367608

Saldana E, Feliciano M, Mugnaini E. 1996. Distribution of descending projections from primary auditory neocortex to inferior colliculus mimics the topography of intracollicular projections. *Journal of Comparative Neurology* 371: 15-40. DIO: https://doi.org/10.1002/(SICI)1096-9861(19960715)371:1<15::AID-CNE2>3.0.CO;2-O, PMID: 8835717

Schmitt TTX, Andrea KMA, Wadle SL, Hirtz JJ. 2023. Distinct topographic organization and network activity patterns of corticocollicular neurons within layer 5 auditory cortex. *Front Neural Circuits* 17: 1210057. DIO: https://doi.org/10.3389/fncir.2023.1210057, PMID: 37521334

Schneider DM, Woolley SM. 2013. Sparse and background-invariant coding of vocalizations in auditory scenes. *Neuron* 79: 141-52. DIO: https://doi.org/10.1016/j.neuron.2013.04.038, PMID: 23849201

Schreiner CE, Sutter ML. 1992. Topography of excitatory bandwidth in cat primary auditory cortex: single-neuron versus multiple-neuron recordings. *Journal of Neurophysiology* 68: 1487-502. DIO: https://doi.org/10.1152/jn.1992.68.5.1487, PMID: 1479426

Scott BB, Thiberge SY, Guo C, Tervo DGR, Brody CD, Karpova AY, Tank DW. 2018. Imaging Cortical Dynamics in GCaMP Transgenic Rats with a Head-Mounted Widefield Macroscope. *Neuron* 100: 1045-1058 e5. DIO: https://doi.org/10.1016/j.neuron.2018.09.050, PMID: 30482694

Shepherd GMG, Yamawaki N. 2021. Untangling the cortico-thalamo-cortical loop: cellular pieces of a knotty circuit puzzle. *Nature Reviews Neuroscience* 22: 389-406. DIO: https://doi.org/10.1038/s41583-021-00459-3, PMID: 33958775

Sherman SM, Guillery RW. 1998. On the actions that one nerve cell can have on another: distinguishing "drivers" from "modulators". *Proceedings of the National Academy of Sciences of the United States of America* 95: 7121-6. DIO: https://doi.org/10.1073/pnas.95.12.7121, PMID: 9618549

Simon E, Perrot X, Mertens P. 2009. [Functional anatomy of the cochlear nerve and the central auditory system]. *Neuro-Chirurgie* 55: 120-6. DIO: https://doi.org/10.1016/j.neuchi.2009.01.017, PMID: 19304300

Smith KR, Wever EG. 1949. The problem of stimulation deafness; the functional and histological effects of a high-frequency stimulus. *Journal of Experimental Psychology* 39: 238-41. DIO: https://doi.org/10.1037/h0061044, PMID: 18125722

Stebbings KA, Lesicko AM, Llano DA. 2014. The auditory corticocollicular system: molecular and circuit-level considerations. *Hearing Research* 314: 51-9. DIO: https://doi.org/10.1016/j.heares.2014.05.004, PMID: 24911237

Stiebler I, Neulist R, Fichtel I, Ehret G. 1997. The auditory cortex of the house mouse: left-right differences, tonotopic organization and quantitative analysis of frequency representation. *J Comp Physiol A* 181: 559-71. DIO: https://doi.org/10.1007/s003590050140, PMID: 9449817

Sun L, Tang Y, Yan K, Yu J, Zou Y, Xu W, Xiao K, Zhang Z, Li W, Wu B, Hu Z, Chen K, Fu ZF, Dai J, Cao G. 2019. Differences in neurotropism and neurotoxicity among retrograde viral tracers. *Molecular Neurodegeneration* 14: 8. DIO: https://doi.org/10.1186/s13024-019-0308-6, PMID: 30736827

Sutter ML, Schreiner CE. 1995. Topography of intensity tuning in cat primary auditory cortex: single-neuron versus multiple-neuron recordings. *Journal of Neurophysiology* 73: 190-204. DIO: https://doi.org/10.1152/jn.1995.73.1.190, PMID: 7714564

Takasaki K, Abbasi-Asl R, Waters J. 2020. Superficial Bound of the Depth Limit of Two-Photon Imaging in Mouse Brain. *eNeuro* 7 DIO: https://doi.org/10.1523/ENEURO.0255-19.2019, PMID: 31907211

Tani T, Abe H, Hayami T, Banno T, Miyakawa N, Kitamura N, Mashiko H, Ichinohe N, Suzuki W. 2018. Sound Frequency Representation in the Auditory Cortex of the Common Marmoset Visualized Using Optical Intrinsic Signal Imaging. *eNeuro* 5 DIO: https://doi.org/10.1523/ENEURO.0078-18.2018, PMID: 29736410

Tao C, Zhang G, Zhou C, Wang L, Yan S, Tao HW, Zhang LI, Zhou Y, Xiong Y. 2017. Diversity in Excitation-Inhibition Mismatch Underlies Local Functional Heterogeneity in the Rat Auditory Cortex. *Cell Rep* 19: 521-531. DIO: https://doi.org/10.1016/j.celrep.2017.03.061, PMID: 28423316

Thomas H, Tillein J, Heil P, Scheich H. 1993. Functional organization of auditory cortex in the mongolian gerbil (Meriones unguiculatus). I. Electrophysiological mapping of frequency representation and distinction of fields. *European Journal of Neuroscience* 5: 882-97. DIO: https://doi.org/10.1111/j.1460-9568.1993.tb00940.x, PMID: 8281300

Thomson AM. 2010. Neocortical layer 6, a review. *Front Neuroanat* 4: 13. DIO: https://doi.org/10.3389/fnana.2010.00013, PMID: 20556241

Tischbirek C, Birkner A, Jia H, Sakmann B, Konnerth A. 2015. Deep two-photon brain imaging with a red-shifted fluorometric Ca2+ indicator. *Proceedings of the National Academy of Sciences of the United States of America* 112: 11377-82. DIO: https://doi.org/10.1073/pnas.1514209112, PMID: 26305966

Tischbirek CH, Noda T, Tohmi M, Birkner A, Nelken I, Konnerth A. 2019. In Vivo Functional Mapping of a Cortical Column at Single-Neuron Resolution. *Cell Rep* 27: 1319-1326 e5. DIO: https://doi.org/10.1016/j.celrep.2019.04.007, PMID: 31042460

Triarhou LC. 2021. Pre-Brodmann pioneers of cortical cytoarchitectonics I: Theodor Meynert, Vladimir Betz and William Bevan-Lewis. *Brain Structure and Function* 226: 49-67. DIO: https://doi.org/10.1007/s00429-020-02168-6, PMID: 33165657

Wang M, Liao X, Li R, Liang S, Ding R, Li J, Zhang J, He W, Liu K, Pan J, Zhao Z, Li T, Zhang K, Li X, Lyu J, Zhou Z, Varga Z, Mi Y, Zhou Y, Yan J, Zeng S, Liu JK, Konnerth A, Nelken I, Jia H, Chen X. 2020. Single-neuron representation of learned complex sounds in the auditory cortex. *Nature Communications* 11: 4361. DIO: https://doi.org/10.1038/s41467-020-18142-z, PMID: 32868773

Wang M, Liu K, Pan J, Li J, Sun P, Zhang Y, Li L, Guo W, Xin Q, Zhao Z, Liu Y, Zhou Z, Lyu J, Zheng T, Han Y, Zhang C, Liao X, Zeng S, Jia H, Chen X. 2022. Brain-wide projection reconstruction of single functionally defined neurons. *Nature Communications* 13: 1531. DIO: https://doi.org/10.1038/s41467-022-29229-0, PMID: 35318336

Watkins PV, Barbour DL. 2011. Rate-level responses in awake marmoset auditory cortex. *Hearing Research* 275: 30-42. DIO: https://doi.org/10.1016/j.heares.2010.11.011, PMID: 21145961

Williamson RS, Polley DB. 2019. Parallel pathways for sound processing and functional connectivity

among layer 5 and 6 auditory corticofugal neurons. *Elife* 8 DIO: https://doi.org/10.7554/eLife.42974, PMID: 30735128

Winer JA, Diehl JJ, Larue DT. 2001. Projections of auditory cortex to the medial geniculate body of the cat. *Journal of Comparative Neurology* 430: 27-55. DIO, PMID: 11135244

Winer JA, Miller LM, Lee CC, Schreiner CE. 2005. Auditory thalamocortical transformation: structure and function. *Trends in Neurosciences* 28: 255-63. DIO: https://doi.org/10.1016/j.tins.2005.03.009, PMID: 15866200

Winkowski DE, Kanold PO. 2013. Laminar transformation of frequency organization in auditory cortex. *J Neurosci* 33: 1498-508. DIO: https://doi.org/10.1523/jneurosci.3101-12.2013, PMID: 23345224

Wu GK, Li P, Tao HW, Zhang LI. 2006. Nonmonotonic synaptic excitation and imbalanced inhibition underlying cortical intensity tuning. *Neuron* 52: 705-15. DIO: https://doi.org/10.1016/j.neuron.2006.10.009, PMID: 17114053

Yarmohammadi H, Mahmoudi Nezhad GS, Dalfardi B, Ghanizadeh A. 2014. Theodor Meynert (1833-1892). *Journal of Neurology* 261: 1647-8. DIO: https://doi.org/10.1007/s00415-013-7077-x, PMID: 23963472

Zeng HH, Huang JF, Chen M, Wen YQ, Shen ZM, Poo MM. 2019. Local homogeneity of tonotopic organization in the primary auditory cortex of marmosets. *Proceedings of the National Academy of Sciences of the United States of America* 116: 3239-3244. DIO: https://doi.org/10.1073/pnas.1816653116, PMID: 30718428

Zhu X, Lin K, Liu Q, Yue X, Mi H, Huang X, He X, Wu R, Zheng D, Wei D, Jia L, Wang W, Manyande A, Wang J, Zhang Z, Xu F. 2020. Rabies Virus Pseudotyped with CVS-N2C Glycoprotein as a Powerful Tool for Retrograde Neuronal Network Tracing. *Neurosci Bull* 36: 202-216. DIO: https://doi.org/10.1007/s12264-019-00423-3, PMID: 31444652

Zingg B, Chou XL, Zhang ZG, Mesik L, Liang F, Tao HW, Zhang LI. 2017. AAV-Mediated Anterograde Transsynaptic Tagging: Mapping Corticocollicular Input-Defined Neural Pathways for Defense Behaviors. *Neuron* 93: 33-47. DIO: https://doi.org/10.1016/j.neuron.2016.11.045, PMID: 27989459